

Uncertainty Awareness on Unsupervised Domain Adaptation for Time Series Data

Weide Liu, Xiaoyang Zhong, Lu Wang, Jingwen Hou, Yuemei Luo, Jiebin Yan, and Yuming Fang

Abstract—Unsupervised domain adaptation methods seek to generalize effectively on unlabeled test data, especially when encountering the common challenge in time series data that distribution shifts occur between training and testing datasets. In this paper, we propose incorporating multi-scale feature extraction and uncertainty estimation to improve the model’s generalization and robustness across domains. Our approach begins with a multi-scale mixed input architecture that captures features at different scales, increasing training diversity and reducing feature discrepancies between the training and testing domains. Based on the mixed input architecture, we further introduce an uncertainty awareness mechanism based on evidential learning by imposing a Dirichlet prior on the labels to facilitate both target prediction and uncertainty estimation. The uncertainty awareness mechanism enhances domain adaptation by aligning features with the same labels across different domains, which leads to significant performance improvements in the target domain. Additionally, our uncertainty-aware model demonstrates a much lower Expected Calibration Error (ECE), indicating better-calibrated prediction confidence. Our experimental results show that this combined approach of mixed input architecture with the uncertainty awareness mechanism achieves state-of-the-art performance across multiple benchmark datasets, underscoring its effectiveness in unsupervised domain adaptation for time series data. Our code is available at <https://github.com/ZhongAobo/Evidential-HAR>.

Index Terms—Human activity recognition, Uncertainty estimation, Evidential learning, Dirichlet prior, Multi-scale time series

I. INTRODUCTION

In various real-world applications such as healthcare and manufacturing, classifying time series data is increasingly critical. Deep learning, in particular, has been gaining attention for its ability to learn the temporal dynamics embedded in complex data patterns, assuming an abundance of labeled data is available [1]. However, labeling this data is often complicated and demanding because it requires specialized domain knowledge [2]. One approach to alleviate the burden of labeling involves using annotated data from a related domain that is already labeled or easier to label, known as the source domain, to train the model, which is then tested on a different

Weide Liu is with College of Computing and Data Science, Nanyang Technological University (NTU), Singapore 639798 (e-mail: weide001@e.ntu.edu.sg).

X Zhong, J Hou, J Yan and Y Fang are with School of Computing and Artificial Intelligence, Jiangxi University of Finance and Economics, China, email: zhongaobo429@foxmail.com, jingwen003@e.ntu.edu.sg, jiebinyan@foxmail.com, fa0001ng@e.ntu.edu.sg

L Wang is with Institute for Infocomm Research (I²R), A*STAR, Singapore, email: wang_lu@i2r.a-star.edu.sg

Y Luo is with School of Artificial Intelligence, Nanjing University of Information Science and Technology, China, email: luoy0021@e.ntu.edu.sg

Corresponding author: Lu Wang. (e-mail: wang_lu@i2r.a-star.edu.sg)

target domain of interest. This strategy can be problematic due to the potentially distinct data distributions between the source and target domains, which might result in significant domain shifts that compromise the model’s performance on the target domain. This challenge is common in time series classification tasks such as Human Activity Recognition (HAR) [3] and Sleep Stage Classification (SSC) [4]. Specifically, Human Activity Recognition (HAR) entails detecting human activities through data collected from embedded sensors in devices like smartphones and wearables, or sensors installed in the environment. HAR has wide-ranging applications, including health monitoring, elderly care, sports training, and interactive games [3]. Similarly, sleep stage classification (SSC) classifies various sleep stages using physiological signals, which is essential for diagnosing sleep disorders and analyzing sleep patterns [5]. However, variations in sensor placement or patient physiology can introduce distribution mismatches that hinder generalization [4].

Differences in temporal characteristics and operational conditions between training and testing datasets often lead to a marked decline in the performance of deep learning models. This challenge, known as the domain shift problem, undermines the efficacy of deep learning in real-world time series applications. Unsupervised Domain Adaptation (UDA) aims to mitigate this issue by adapting models trained on a labeled source domain to perform effectively on an unlabeled, shifted target domain. While there is extensive research on UDA for visual tasks [6]–[8], its application to time series data remains comparatively underexplored.

Current methodologies for time series domain adaptation typically align source and target domains by minimizing statistical discrepancies (e.g., via distribution matching [9]–[12]) or leveraging adversarial training with domain discriminators [13]–[16]. While these approaches encourage feature robustness across domains, they often overlook a critical factor: model uncertainty. In real-world scenarios, domain shifts introduce ambiguity in how well-aligned features generalize to the target domain. Without explicitly quantifying uncertainty, models risk overconfident predictions on poorly adapted regions of the target data, leading to unreliable performance. Uncertainty estimation thus becomes indispensable for evaluating a model’s generalization capacity and identifying adaptation gaps caused by temporal variations in sensor conditions.

To address these challenges, we propose a novel unsupervised domain adaptation (UDA) framework that integrates multi-scale temporal modeling with evidential uncertainty-aware learning. First, our mixed multi-scale architecture captures hierarchical temporal patterns (e.g., short-term fluctua-

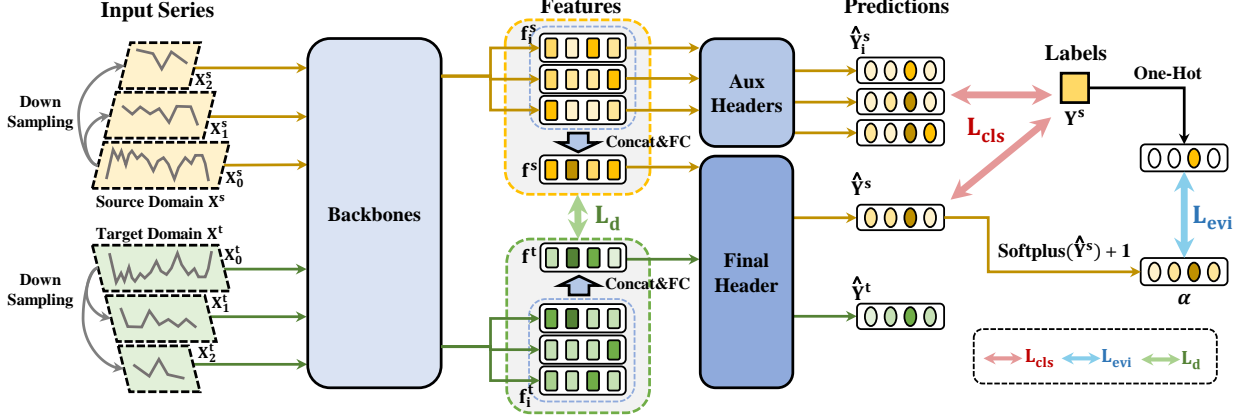


Fig. 1: The architecture of our method. Where L_d is domain loss, L_{cls} is classifier loss, and L_{evi} is our evidential loss. f_i^s and f_i^t are features of the images for the source domain and target domain at scale i . ‘Aux Headers’ refers to the auxiliary classification heads for different scales and ‘Final Header’ is the final classification head using all concatenated features of different scales.

tions and long-term trends), enabling robust feature extraction for domain-varying signals. By processing data across scales, the model reduces ambiguity in temporal representations, critical for adaptation tasks where domain shifts occur at specific frequencies. Second, we incorporate evidential learning [17], [18] to estimate epistemic uncertainty, which quantifies prediction confidence. Unlike traditional probabilistic methods, evidential learning models uncertainty through evidence accumulation, treating network outputs as parameters of a Dirichlet distribution (conjugate to the categorical distribution). This approach avoids reliance on softmax-based point estimates and optimizes predictions via an evidential Bayesian risk loss, directly reflecting uncertainty during domain transfer.

The synergy of these components ensures robust alignment between domains while identifying samples of high uncertainty (e.g., irregular patterns or unseen dynamics) where adaptation may falter. By prioritizing uncertain samples during training, the framework refines feature representations, enhancing robustness against temporal shifts. For instance, in applications like HAR or SSC, where sensor heterogeneity or physiological variability induce uncertainty, the model adapts cautiously to ambiguous target data, avoiding overconfidence. Experiments across five time series datasets demonstrate that our method achieves state-of-the-art performance, balancing predictive accuracy with interpretable uncertainty quantification for reliable cross-domain adaptation. The main contributions of this paper are summarized as follows:

- We introduce a novel framework that incorporates uncertainty awareness for time series classification, enhancing predictive accuracy and reliability.
- We advocate for the use of mixed-length time series data as input, improving the model’s ability to learn from diverse patterns and cycles, thus enhancing the robustness of time series classification tasks.
- Our experimental evaluations across five distinct datasets—UCIHAR, WISDM, HHAR, SSC, and MFD—show that our method achieves a new state-of-the-art.

Parts of the results in this paper were previously presented in its workshop version, which received the Best Paper Award at the 4th International Workshop on Deep Learning for Human Activity Recognition, IJCAI 2024 [20]. This paper significantly extends our earlier work in several crucial aspects:

- We extend the proposed algorithm with using of mixed-length time series data encoded by Multi-scale Mixing Architecture as input, improving the model’s ability to learn from diverse patterns and cycles, thus enhancing the robustness of time series classification tasks.
- We conduct a new experiment on new tasks such as sleep stage classification, and machine fault diagnosis to further evaluate our algorithm.
- We extend the investigation to new tasks including the Sleep Stage Classification (SSC) [4] and Machine Fault Diagnosis (MFD) [21].
- Additionally, we have broadened our research framework by incorporating new analytical tasks. These enhancements are aimed at refining our experimental methods through the use of confusion matrices and model uncertainty assessments, as shown in Figures 3, 6, and 8. We also explore the shift in data distribution between the source and target datasets, illustrated in Figures 4 and 5. Furthermore, we conduct detailed performance comparisons (Figure 9), analyze Expected Calibration Error (ECE) in Figure 7, and use t-SNE to visualize features extracted by various methods (Figure 10). Additionally, we assess the distribution of data through Principal Component Analysis (PCA) on model uncertainty, depicted in Figure 11. These approaches enhance the depth and accuracy of our evaluation, allowing for a more comprehensive understanding of the robustness of deep learning models in time series classification.
- We analyze the performance of the overall datasets and tasks, as shown in Tables I and II, to provide a comprehensive evaluation of our algorithm.

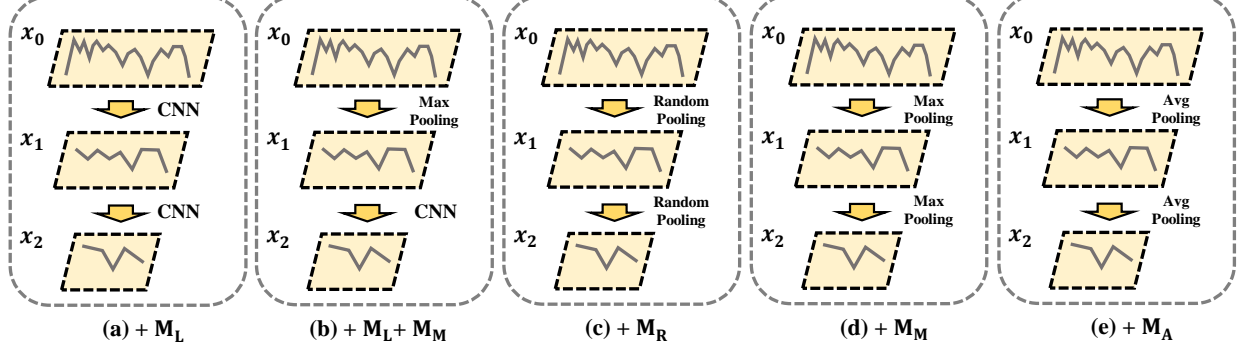


Fig. 2: Different down-sampling method in our multi-scale mixing architecture, where (a) denotes down-sampling with the 1D CNN, (b) denotes down-sampling with the 1D CNN and max-pooling, (c) denotes down-sampling with the random-pooling, (d) denotes down-sampling with the max-pooling and (e) denotes down-sampling with the avg-pooling.

TABLE I: The table presents a comparison of our method with other approaches, where the performance of the baseline model is benchmarked against AdaTime [19]. Uncertainty is imposed by two different priors, i.e., the normal-inverse-gamma (NIG) distribution with normal likelihood [18] and the Dirichlet (DIR) distribution with categorical likelihood [17]. The ml , ce , mse correspond to 3 different losses according to Equation (4), Equation (5) and Equation (6), respectively. The Bayesian risk loss with cross-entropy shows the best f1 score on average.

Dataset	Method	noAdapt	DDC	Deep	HoMM	DANN	MMDA	DSAN	CDAN	DIRT	CoDATS	AdvSKM	SASA	CLUDA	AVG
UCI HAR	Baseline	65.94	82.29	86.30	88.52	88.26	89.39	91.46	90.72	93.68	88.20	80.10	85.00	91.47	86.26
	+NIG	70.34	87.61	89.33	87.63	87.72	88.56	92.23	88.57	91.36	88.11	87.01	83.87	90.98	87.26
	+DIR _{ml}	82.69	88.61	89.86	91.77	89.58	90.31	90.51	90.40	92.90	91.33	88.14	87.55	91.88	89.66
	+DIR _{mse}	78.40	88.15	90.07	92.11	89.76	90.28	92.36	90.51	93.12	92.87	88.39	86.40	91.57	89.54
	+DIR _{ce}	80.99	88.49	89.61	91.77	89.55	89.98	92.43	91.79	93.72	91.97	88.05	88.37	91.97	89.90
WISDM	Baseline	48.60	53.78	54.19	56.92	62.41	59.82	61.08	55.59	59.59	62.06	54.82	53.34	57.36	56.89
	+NIG	50.01	53.57	53.50	51.01	57.02	60.68	57.62	52.96	59.46	58.67	53.61	54.05	57.31	55.34
	+DIR _{ml}	55.91	58.03	58.21	57.72	66.00	61.15	63.12	56.92	60.20	62.11	51.95	53.17	57.75	58.63
	+DIR _{mse}	55.56	58.34	58.46	60.12	60.01	61.84	64.23	61.05	60.65	62.25	55.09	53.50	57.65	59.13
	+DIR _{ce}	53.46	57.52	58.46	60.18	62.76	61.22	61.71	59.56	61.03	63.93	58.33	54.57	57.41	59.24
HHAR	Baseline	63.07	68.29	71.75	73.69	77.89	76.93	79.27	79.07	80.47	76.41	65.88	75.76	78.12	74.35
	+NIG	64.55	69.99	70.25	71.54	78.86	76.10	77.93	72.82	80.81	74.84	67.28	77.37	77.12	73.80
	+DIR _{ml}	68.08	70.51	73.27	76.15	80.15	79.67	78.92	78.81	81.46	79.58	68.81	76.50	78.13	76.16
	+DIR _{mse}	66.87	69.12	73.18	75.99	79.68	79.73	79.29	78.12	82.91	78.62	68.71	76.16	78.31	75.90
	+DIR _{ce}	67.84	70.20	73.26	76.23	79.78	78.08	79.98	79.87	82.39	78.84	69.10	77.67	78.65	76.30
SSC	Baseline	51.67	60.88	61.05	60.81	60.80	63.47	59.51	61.38	57.32	61.18	59.81	59.59	59.77	
	+NIG	51.52	61.24	60.39	60.48	60.50	63.99	59.69	59.32	61.22	56.54	61.14	59.19	59.59	59.60
	+DIR _{ml}	54.87	59.73	61.24	59.29	58.58	63.58	59.06	62.14	58.73	61.69	60.81	58.70	59.65	59.85
	+DIR _{mse}	55.30	60.29	61.54	59.57	58.81	63.03	60.24	62.27	58.80	61.84	61.46	58.71	59.75	60.12
	+DIR _{ce}	54.88	60.02	61.29	60.05	59.39	63.43	59.78	61.98	58.59	62.15	61.18	59.40	59.85	60.15
MFD	Baseline	72.51	81.54	80.80	81.18	84.06	85.44	81.65	84.64	92.81	84.20	81.47	78.94	92.22	83.19
	+NIG	73.44	83.59	80.82	83.28	85.93	85.75	82.54	86.60	94.46	83.99	83.70	78.52	91.66	84.17
	+DIR _{ml}	80.90	89.64	88.80	87.06	96.52	97.75	90.66	87.77	89.57	90.42	88.86	90.61	93.12	90.13
	+DIR _{mse}	81.00	89.80	89.06	87.51	96.21	97.87	90.57	87.04	89.98	90.11	89.04	90.74	92.34	90.10
	+DIR _{ce}	81.34	90.53	89.53	87.71	96.32	97.56	90.95	87.80	90.04	90.88	88.74	91.12	93.08	90.43

II. RELATED WORK

A. Unsupervised Domain Adaptation

Classical domain adaptation methods mitigate domain shift by aligning feature distributions between source and target domains. Techniques like CORAL [22] align second-order statistics (e.g., covariance matrices) to reduce linear discrepancies, while TCA [23] projects data into a latent subspace using kernel methods to handle nonlinear shifts. Feature alignment methods minimize divergence metrics (e.g., MMD) or reweight samples to learn domain-invariant representations. However, these approaches often rely on shallow or linear transformations, limiting their ability to model complex, high-dimensional data. They may also require explicit domain labels, struggle with large domain gaps, and lack robustness to noisy target domains. Modern deep adaptation frameworks extend these ideas by leveraging deep networks to learn hierarchical, transferable features through adversarial training or deep alignment objectives.

B. Unsupervised Domain Adaptation for Time Series

The time series classification tasks [24]–[29] frequently exhibit significant domain shifts. This occurs when models trained on data from one subject (source domain) are applied to data from another (target domain).

While there have been significant achievements in computer vision, the adaptation of these successes to human activity recognition data remains limited. VRADA [30] leverages a variational recurrent neural network (VRNN) and employs adversarial training to capture complex, domain-invariant temporal relationships. Building on VRADA, CoDATS [31] utilizes a convolutional neural network (CNN) as the feature extractor to enhance this methodology. Methods such as SASA [32] strive to align the conditional distribution of human activity recognition data by reducing the discrepancies in the associative structures of time series variables across domains. AdvSKM [16] and related works [33] employ metric-based approaches to align domains based on statistical divergence.

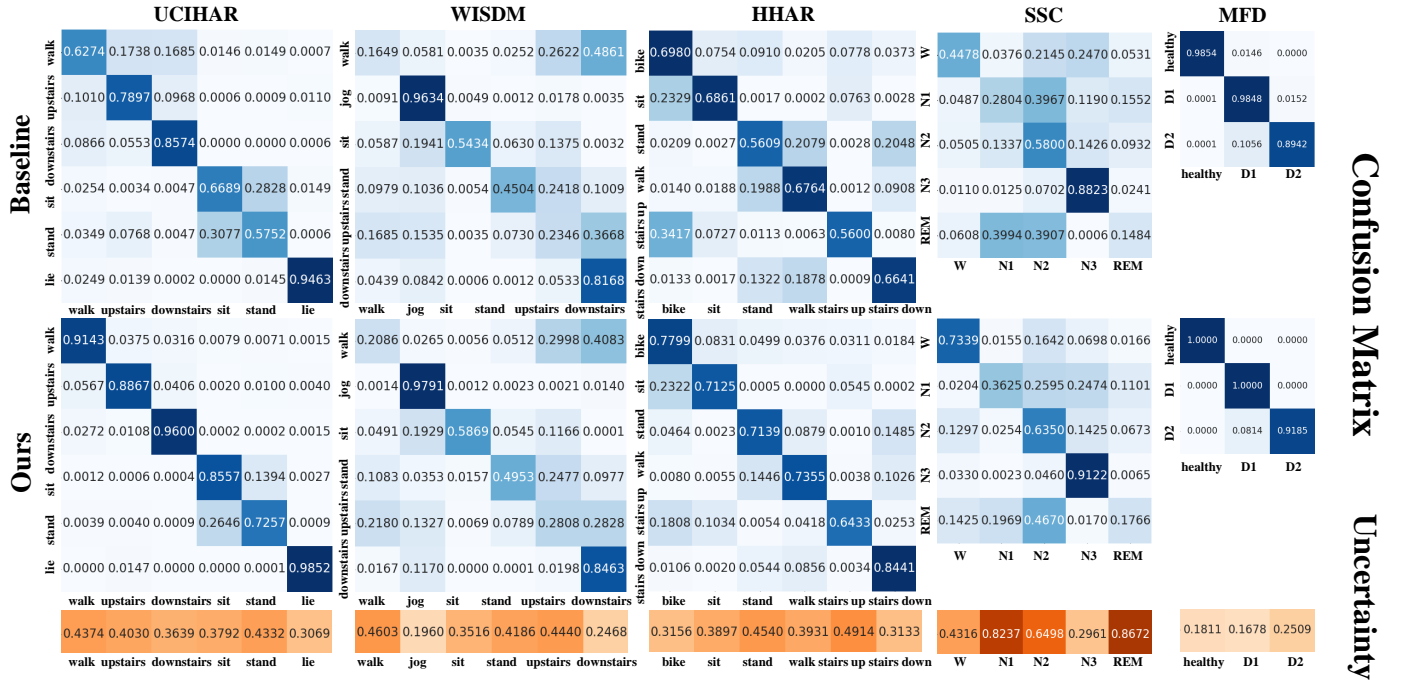


Fig. 3: The confusion matrix and uncertainty. Using the noAdapt method as the baseline, test on 5 different datasets.

Techniques like DAF [34] extract both domain-invariant and domain-specific features, utilizing a shared attention module with a reconstruction task for forecasting across source and target domains. Contrastive DA methods such as CLUDA [35] and CLADA [36] employ augmentations to extract domain-invariant and contextual features for prediction. Furthermore, Maekawa *et al.* [37] introduced an unsupervised method that identifies individual iterations of assembly work using acceleration data. However, the application of evidential learning to domain adaptation for human activity recognition remains unexplored. In our research, we apply evidential learning to the task of human activity recognition, with the objective of improving both the accuracy and reliability of the results.

C. Uncertainty Estimation

With the rapid development of deep learning [27], [29], [38], [39], estimating uncertainty in machine learning models has gained considerable attention, particularly in safety-critical domains such as autonomous vehicle navigation and medical diagnostics. This research explores uncertainty in two primary forms: aleatoric and epistemic. Aleatoric uncertainty, inherent in the observations like sensor noise, is contrasted with epistemic uncertainty, which pertains to model parameters and can decrease with additional data [40].

Bayesian modeling highlights the significant memory and computational demands of traditional methods, often rendering them impractical. In response, some strategies involve training sub-networks with shared parameters, merging their outputs to address these limitations [41]. Conversely, deterministic techniques provide direct uncertainty estimates, reducing model overconfidence [42].

Murat *et al.* [17] introduce a method to enhance prediction confidence by explicitly modeling prediction uncertainty

through subjective logic and a Dirichlet distribution on class probabilities. This approach, distinct from conventional methods focused solely on minimizing prediction loss or Bayesian networks, shows enhanced performance in managing out-of-distribution queries and withstanding adversarial attacks.

In this paper, we propose employing these uncertainty estimation techniques for unsupervised domain adaptation in human activity recognition tasks, aiming to leverage these methodologies to improve model reliability and performance in critical applications.

III. METHODS

A. Task Definition

In this paper, we delineate the concept of unsupervised domain adaptation (UDA). The scenario considered involves access to labeled data from a source domain $X^s = \{x_i^s, y_i^s\}_{i=1}^{N_s}$, encompassing either univariate or multivariate human activity recognition data, and unlabeled data from a target domain $X^t = \{x_j^t\}_{j=1}^{N_t}$. Here, N_s and N_t signify the number of samples in the source and target domains, respectively. Our focus is on classification tasks, with the assumption that both domains share the same set of labels, denoted by $Y = \{1, 2, \dots, K\}$, where K represents the total number of classes.

Following data preprocessing methods [19], we divide the source domain into a training subset X_{tr}^s with N_{tr}^s samples, and a test subset X_{te}^s with N_{te}^s samples. Similarly, the target domain is partitioned into a training subset X_{tr}^t with N_{tr}^t samples, and a test subset X_{te}^t with N_{te}^t samples. It is essential to note that the source and target domains are characterized by distinct marginal distributions, denoted as $P_s(x) \neq P_t(x)$, although the conditional distribution is assumed to remain consistent, i.e., $P_s(y|x) = P_t(y|x)$.

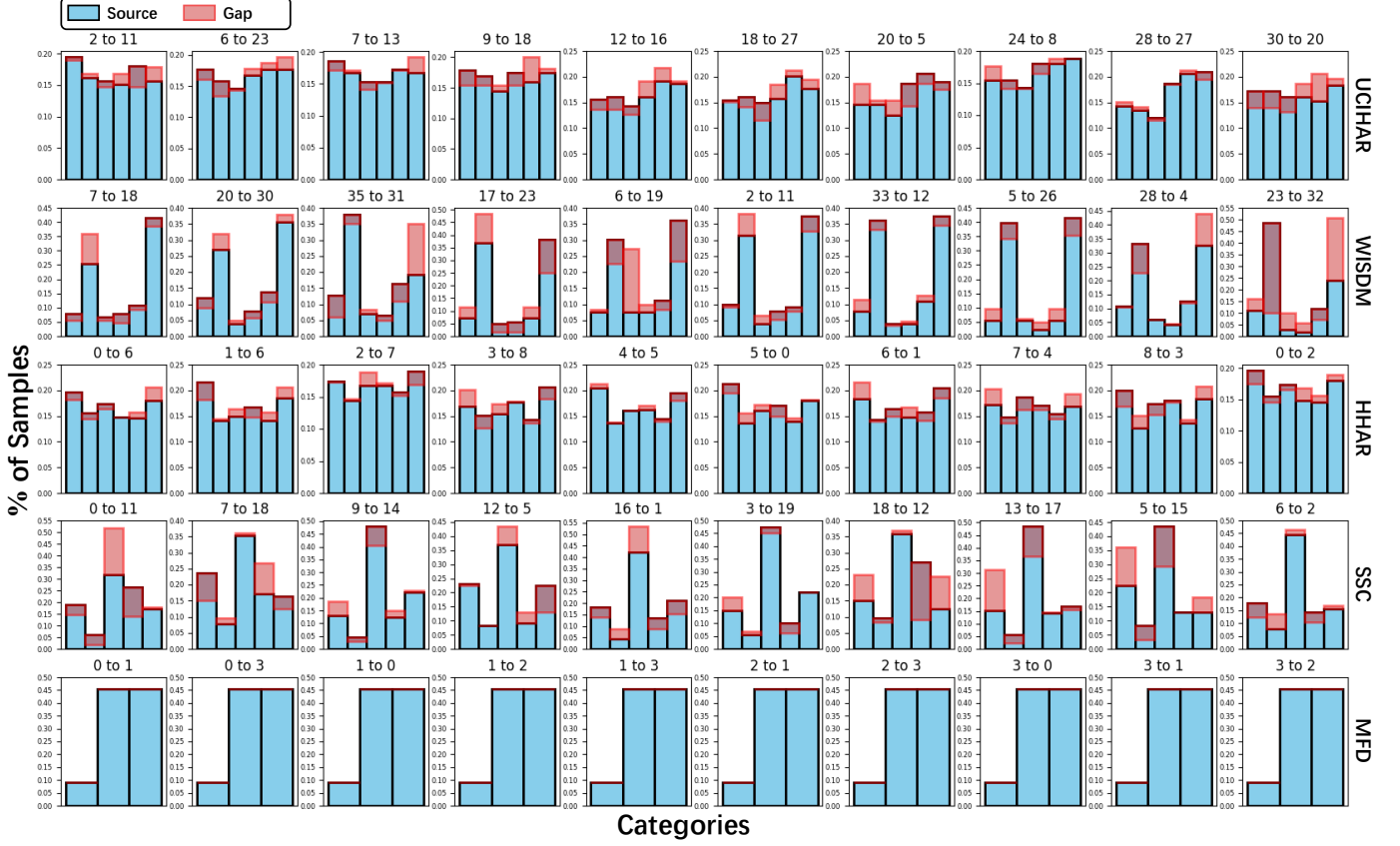


Fig. 4: This figure illustrates the label distribution of source data across various dataset splits, along with the gap (indicated by red) between the distributions of source and target data. The x axis represents the different categories, while the y axis represents the distribution density. As shown in the figure, we demonstrate the variations in sample quantities across different categories within five datasets and also emphasize the discrepancies in category distributions between the source and target domains.

The primary objective of UDA is to minimize the discrepancy between the distributions $P_s(x)$ and $P_t(x)$, under the premise that the label spaces are identical across the domains. Denote the discrepancy between the marginal distributions $P_s(x)$ and $P_t(x)$ as L_d . One can typically use the different orders of data distribution statistics to calculate L_d . A combined loss of source classification L_{cls} and the domain alignment L_d is jointly optimized to train a model $M = h(f(\theta))$ with a feature extractor $f(\theta)$ and a classifier $h(\theta)$ as typically shown in Figure 1. The combined loss L_{uda} achieves a certain balance between the accuracy of the prediction in the source and the regularization of domain alignment:

$$L_{uda} = \lambda_1 L_{cls} + \lambda_2 L_d, \quad (1)$$

where λ_1 and λ_2 are the regularization parameters.

B. The Multi-scale Mixing Architecture

Time series data exhibit unique characteristics at different scales; fine scales capture detailed patterns while coarse scales are indicative of broader, macroscopic variations [43]. This multi-scale perspective is crucial as it helps disentangle the intricate variations inherent in temporal data, which is particularly beneficial for modeling temporal variations in time

series classification tasks. We introduce the Multi-scale Mixing Architecture, a novel architecture designed for multi-scale time series analysis that optimally utilizes both past data extraction and future prediction, as shown in Figure 1. The initial step involves downsampling the entire time sequence, represented as $x \in \mathbb{R}^{P \times C}$, into multiple scales through average pooling, resulting in a set of multi-scale time series $X = \{x_0, \dots, x_M\}$, where $x_m \in \mathbb{R}^{\lfloor \frac{P}{2^m} \rfloor \times C}$ for $m \in \{0, \dots, M\}$, and C denotes the number of variables.

Subsequently, we individually encode and decode the multi-scale features f_i , then integrate these feature maps for the final prediction. The series $x_0 = x$ represents the finest temporal variations as the input series, while the highest-level series x_M captures macroscopic variations. These multi-scale series are transformed into deep features, independently optimized, and then aggregated into final feature maps for prediction and are the main components for calculating the L_{cls} after through a classification header. Additionally, auxiliary classification losses from features at different scales are introduced through auxiliary heads to support the training process. These auxiliary losses help guide the model in learning more effectively from multi-scale features. Together with the main classification component, the final classification loss, L_{cls} , is composed of

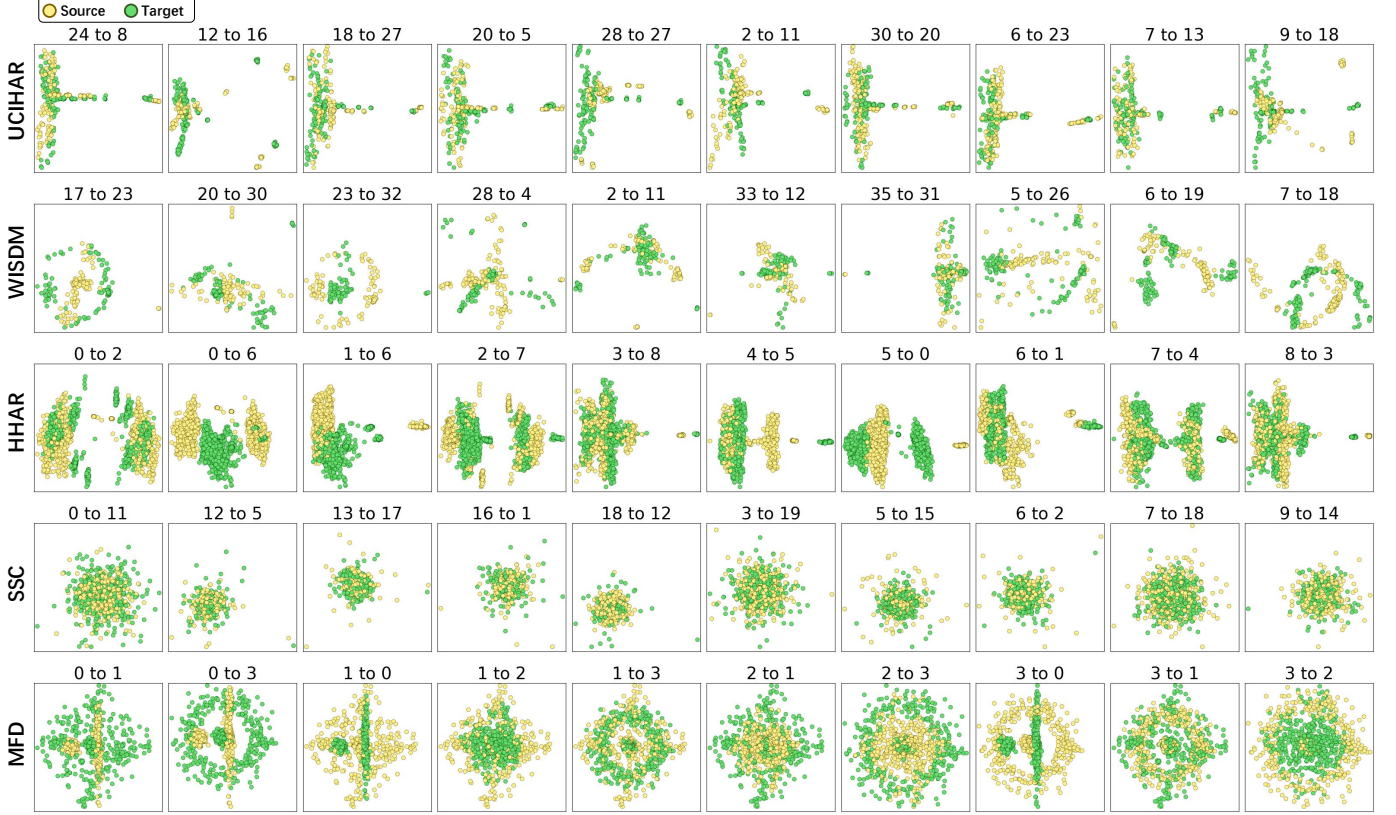


Fig. 5: The PCA visualization of samples of different domains across 10 splits (source and target samples are shown in yellow and green). Distribution shifts are evident between the source and target samples.

multiple terms:

$$L_{cls} = L_{cls}^{Y^s} + \lambda_i \sum L_{cls}^{Y_i^s},$$

where for $i \in \{0, 1, 2\}$, λ_i takes the values $\{0.5, 0.25, 0.25\}$ in our experiments. As illustrated in Fig. 1, $L_{cls}^{Y^s}$ is the classification loss using the combined feature from all scales from the ‘‘Final Header’’, while $L_{cls}^{Y_i^s}$ is the classification loss at different scale from ‘‘Aux Headers’’. This method ensures a comprehensive representation of the input series across different scales, thereby optimizing both the fidelity of temporal pattern recognition and the predictive accuracy of the model.

In this paper, we explore different down-sampling strategies, such as CNN-only, max-pooling, random-pooling, and average-pooling, in the multi-scale mixing architecture to handle time series inputs at various resolutions, as shown in Fig. 2, where each subfigure represents a unique combination of down-sampling techniques applied to multi-scale input. It compares five approaches: (a) down-sampling with only 1D CNN layers, (b) combining 1D CNN with max-pooling, (c) using random-pooling after CNN, (d) applying max-pooling alone, and (e) utilizing average-pooling. Each method processes multi-scale inputs (x_0, x_1, x_2) to capture features across varying temporal resolutions, highlighting how different pooling strategies affect feature extraction and down-sampling. Parameters of the different down-sampling methods in Fig. 2 are summarized in Appendix for reproduction.

C. Target Modeling with Uncertainty

In unsupervised domain adaptation (UDA), models are typically trained to align features across domains via adversarial training or distribution matching, as shown in Fig. 1. However, even well-aligned features can correspond to ambiguous or novel patterns, leading to overconfident mispredictions. We argue that UDA frameworks must quantify uncertainty explicitly to identify unreliable predictions caused by domain shifts to ensure calibrated outputs. Building on this principle, we enhance the UDA pipeline in Fig. 1 with evidential learning. Traditional classifiers output softmax probabilities as point estimates, conflating confidence with certainty. Evidential learning instead treats predictions as accumulated evidence under a Dirichlet prior over class probabilities. This approach identifies misaligned or novel samples with high-uncertainty and prioritizes them to learning uncertainty-aware features, enabling cautious adaptation to ambiguous data while reducing overconfidence.

Following the approach of evidential learning for classification introduced in [17], we model the labels with a multinomial/categorical distribution:

$$f(\mathbf{p}|\alpha) = \frac{1}{B(\alpha)} \prod_{k=1}^K p_k^{\alpha_k-1}, \quad (2)$$

where $B(\alpha) = \frac{\prod_{k=1}^K \Gamma(\alpha_k)}{\Gamma(\sum_{k=1}^K \alpha_k)}$ is the K-dimensional multinomial beta function, $\Gamma(\cdot)$ is the Gamma function and $\mathbf{p} \in \mathcal{S}_K$ with

TABLE II: The table presents a comparison of our method with other approaches. Baseline* denotes the results reproduced according to the published code provided by the author. The + UN denotes with the uncertainty awareness, while + M_L denotes the multi-scale mixing architecture with learnable parameter (1D CNN), + M_R denotes the multi-scale mixing architecture with random pooling, + M_M denotes the multi-scale mixing architecture with max pooling, + M_A denotes the multi-scale mixing architecture with averaging pooling (detailed architectures are illustrated in Figure 2).

Dataset	Method	noAdapt	DDC	Deep	HoMM	DANN	MMDA	DSAN	CDAN	DIRT	CoDATS	AdvSKM	SASA	CLUDA	Avg
UCIHAR	Baseline	65.94	82.29	86.30	88.52	88.26	89.39	91.46	90.72	93.68	88.20	80.10	85.00	-	85.82
	Baseline*	70.77	87.55	88.75	90.77	88.36	89.04	91.11	88.20	91.27	88.95	86.74	87.89	91.47	87.76
	+ UN	80.90	88.49	89.61	91.77	89.55	89.98	92.43	91.79	93.72	91.97	88.05	88.37	91.97	89.90
	+ UN + M_L	81.32	90.13	90.82	92.38	91.16	91.07	92.53	92.72	91.32	92.19	90.51	88.77	91.47	90.49
	+ UN + $M_L + M_M$	80.02	91.63	90.19	92.96	92.21	91.85	93.22	93.16	91.45	92.03	90.89	89.11	91.44	90.86
	+ UN + M_R	80.13	92.14	90.21	92.31	92.05	92.45	92.79	93.82	92.00	91.58	92.28	86.46	90.88	90.70
	+ UN + M_M	81.87	92.40	90.76	92.55	92.75	92.56	93.55	93.67	92.64	93.37	92.51	86.87	92.03	91.35
	+ UN + M_A	81.04	92.19	90.72	92.40	92.25	92.51	93.51	93.61	91.85	93.88	92.06	88.56	91.99	91.27
WISDM	Baseline	48.60	53.78	54.19	56.92	62.41	59.82	61.08	55.59	59.59	62.06	54.82	53.34	-	56.85
	Baseline*	47.90	56.41	55.90	53.27	60.63	55.63	59.64	57.79	57.71	62.21	57.92	53.76	57.36	56.63
	+ UN	53.46	57.52	58.46	60.18	62.76	61.22	61.71	59.56	61.03	63.93	58.33	54.57	57.41	59.24
	+ UN + M_L	54.49	62.19	62.12	65.66	67.88	63.29	66.29	62.50	59.26	64.48	62.74	57.97	57.99	62.07
	+ UN + $M_L + M_M$	53.66	61.13	62.99	62.56	67.26	63.58	66.32	59.96	61.37	63.95	64.87	55.64	59.88	61.78
	+ UN + M_R	53.57	61.79	64.97	61.34	66.10	63.98	66.82	59.50	59.90	63.65	65.13	55.22	60.83	61.76
	+ UN + M_M	52.98	60.92	63.24	60.46	66.64	63.82	64.59	58.51	59.12	60.93	61.58	58.98	64.65	61.26
	+ UN + M_A	54.02	63.35	64.68	60.23	69.98	64.95	63.43	58.16	61.33	61.14	61.47	56.07	60.02	61.45
HHAR	Baseline	63.07	68.29	71.75	73.69	77.89	76.93	79.27	79.07	80.47	76.41	65.88	75.76	-	74.04
	Baseline*	62.01	66.97	72.98	75.95	78.56	76.51	77.13	78.10	81.27	74.27	65.91	75.90	78.12	74.13
	+ UN	67.84	70.20	73.26	76.23	79.78	78.08	79.98	79.87	82.39	78.84	69.10	77.67	78.65	76.30
	+ UN + M_L	68.99	70.67	76.51	77.84	79.36	81.64	77.30	79.77	80.51	78.01	69.91	77.02	78.88	76.65
	+ UN + $M_L + M_M$	69.21	70.74	76.54	78.97	78.63	81.87	79.25	79.48	81.02	76.47	69.98	77.03	78.15	76.72
	+ UN + M_R	68.78	70.39	76.14	78.65	78.75	80.85	76.99	80.15	81.21	76.74	70.26	76.34	78.92	76.47
	+ UN + M_M	69.32	69.66	75.87	79.71	81.63	80.54	77.45	80.77	81.33	78.24	70.59	76.48	79.32	76.99
	+ UN + M_A	67.99	71.26	76.15	78.30	79.27	80.76	78.23	79.92	81.42	76.48	69.35	77.07	77.96	76.47
SSC	Baseline	51.67	60.88	61.05	60.81	60.80	63.47	59.51	61.38	57.32	61.18	59.81	-	-	59.78
	Baseline*	51.41	59.84	61.00	59.27	59.23	63.13	59.52	60.36	57.54	61.93	60.07	58.86	59.59	59.37
	+ UN	54.88	60.02	61.29	60.05	59.39	63.43	59.78	61.98	58.59	62.15	61.18	59.40	59.85	60.15
	+ UN + M_L	56.21	62.86	63.25	63.11	63.25	62.54	63.00	62.29	59.85	63.83	61.98	60.28	60.12	61.74
	+ UN + $M_L + M_M$	56.10	61.88	62.97	61.67	61.40	63.07	62.36	62.39	60.56	61.75	59.43	59.59	59.87	61.00
	+ UN + M_R	55.61	61.04	63.53	62.81	62.17	62.62	62.28	63.36	59.69	62.72	61.34	60.88	58.99	61.31
	+ UN + M_M	56.24	61.84	63.07	61.98	61.56	62.06	63.46	62.56	60.13	62.69	60.97	61.03	59.47	61.31
	+ UN + M_A	54.78	59.82	63.51	61.04	61.28	62.31	62.84	61.14	60.11	62.18	60.46	60.38	59.45	60.72
MFD	Baseline	72.51	81.54	80.80	81.18	84.06	85.44	81.65	84.64	92.81	84.20	81.47	78.94	-	82.44
	Baseline*	77.23	88.08	88.19	86.72	96.30	97.27	85.94	87.67	88.51	87.35	88.72	90.17	92.22	88.80
	+ UN	81.34	90.53	89.53	87.71	96.32	97.56	90.95	87.80	90.04	90.88	88.74	91.12	93.08	90.43
	+ UN + M_L	80.99	89.36	94.49	91.72	95.62	94.09	90.64	95.56	95.99	88.40	89.77	89.36	94.02	91.54
	+ UN + $M_L + M_M$	82.03	91.33	93.47	92.67	95.27	95.09	92.92	91.44	96.08	92.06	90.32	92.91	93.02	92.20
	+ UN + M_R	80.45	88.70	94.88	91.78	96.52	95.43	90.89	95.33	90.05	89.16	91.58	88.17	91.98	91.15
	+ UN + M_M	81.23	90.61	93.71	91.03	96.24	94.73	91.47	93.61	94.61	90.08	90.58	89.99	93.33	91.63
	+ UN + M_A	81.88	91.16	95.96	92.14	97.20	96.47	92.68	91.61	91.69	88.78	89.08	90.21	92.58	91.65

\mathcal{S}_K being the K -dimensional unit simplex defined as

$$\mathcal{S}_K = \left\{ \mathbf{p} \mid \sum_{k=1}^K p_k = 1, \text{ with } 0 \leq p_1, \dots, p_k \leq 1 \right\}.$$

The prior reflects our beliefs about the space of possible models and incorporates epistemic uncertainty in the problem formulation. This choice of Dirichlet prior due to its conjugate property with multinomial distribution, enables a close-form Dirichlet posterior and thus efficient inference. The expected probability for the k -th outcome is therefore the mean of the Dirichlet posterior distribution:

$$\mathbb{E}[p_k] = \hat{p}_k = \frac{\hat{\alpha}_k}{S}, \quad (3)$$

where $S = \sum_{k=1}^K \hat{\alpha}_k$ is the total amount of the evidence and $\hat{\alpha}_k$ is updated α_k from the posterior and $\mathbb{E}[\cdot]$ is the operation of expectation.

Both the Type-II Maximum Likelihood in Equation (4) and two different Bayesian risks using cross-entropy error in Equation (5) and mean square error in Equation (6) can be used [17] to design the loss to estimate $\hat{\alpha}_k$ from the network M .

Type-II Maximum Likelihood Loss:

$$L_i^{ml}(\theta) = -\log \left(\int_{k=1}^K p_{ik}^{y_{ik}} \frac{1}{B(\alpha_i)} \prod_{k=1}^K p_{ik}^{\alpha_{ik}} d\mathbf{p}_i \right) = \sum_{k=1}^K y_{ik} (\log(S_i) - \log(\alpha_{ik})), \quad (4)$$

$$L_i^{ce}(\theta) = \int \left[\sum_{k=1}^K -y_{ik} \log(p_{ik}) \right] \frac{1}{B(\alpha_i)} \prod_{k=1}^K p_{ik}^{\alpha_{ik}-1} d\mathbf{p}_i = \sum_{k=1}^K y_{ik} (\varphi(S_i) - \varphi(\alpha_{ik})), \quad (5)$$

where $\varphi(\cdot)$ is the digamma function.

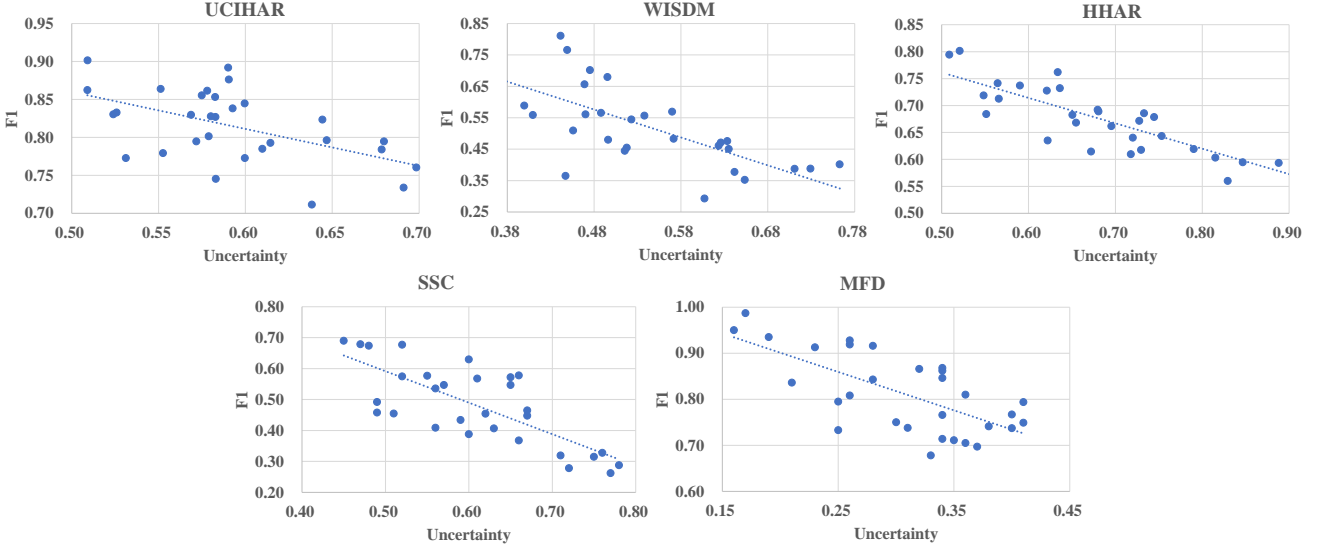


Fig. 6: The correlation between F1 score and uncertainty. The baseline is the basic model without domain adaption, randomly select 10 folds on UCIHAR, WISDM, HHAR, SSC and MFD datasets for test, repeat 30 times.

Bayesian risks using mean square error:

$$\begin{aligned}
 L_i^{mse}(\theta) &= \int \|\mathbf{y}_i - \mathbf{p}_i\|_2^2 \frac{1}{B(\boldsymbol{\alpha}_i)} \prod_{j=1}^K p_{ij}^{\alpha_{ij}-1} d\mathbf{p}_i \\
 &= \sum_{j=1}^K \mathbb{E} [y_{ij}^2 - 2y_{ij}p_{ij} + p_{ij}^2] \\
 &= \sum_{j=1}^K y_{ij}^2 - 2y_{ij}\mathbb{E}[p_{ij}] + \mathbb{E}[p_{ij}^2] \\
 &= \sum_{k=1}^K (y_{ik} - \hat{p}_{ik})^2 + \frac{\hat{p}_{ik}(1 - \hat{p}_{ik})}{S_i + 1} \quad (6)
 \end{aligned}$$

where $\hat{p}_{ik} = \frac{\alpha_{ik}}{S_i}$ is the prediction. The loss L_i^{mse} aims to minimize jointly the prediction error and the variance of the Dirichlet experiment generated by the neural net for each sample i . We tried all three different losses in our experiments and empirically found that the Bayesian risk with cross-entropy error when optimized yields the best performance for our case. Please refer to Table I later in the paper for the performance comparison on difference losses.

Following [17], a Kullback-Leibler (KL) divergence term is further used in the loss function to regularize the predictive distribution space by penalizing parameters α_k that do not contribute to data fit:

$$\begin{aligned}
 &KL[\mathcal{D}(\mathbf{p}_i|\tilde{\boldsymbol{\alpha}}_i)||\mathcal{D}(\mathbf{p}_i|\mathbf{1})] \\
 &= \log \left(\frac{\Gamma\left(\sum_{k=1}^K \tilde{\alpha}_{ik}\right)}{\Gamma(K) \prod_{k=1}^K \Gamma(\tilde{\alpha}_{ik})} \right) \\
 &+ \sum_{k=1}^K (\tilde{\alpha}_{ik} - 1) \left[\varphi(\tilde{\alpha}_{ik}) - \varphi\left(\sum_{j=1}^K \tilde{\alpha}_{ij}\right) \right], \quad (7)
 \end{aligned}$$

where $\mathcal{D}(\mathbf{p}_i|\mathbf{1})$ is the uniform Dirichlet distribution with $\mathbf{1}$ being the K ones vector, and $\tilde{\boldsymbol{\alpha}}_i = \mathbf{y}_i + (1 - \mathbf{y}_i) \cdot \boldsymbol{\alpha}_i$ is the Dirichlet parameters after removal of the non-misleading

evidence from predicted parameters $\boldsymbol{\alpha}_i$ for sample i . Therefore the total evidential loss for α_k estimation is a balance between the Bayesian risk and the KL divergence:

$$L_{evi} = \sum_{i=1}^{N_s} L_i + \lambda_t \sum_{i=1}^{N_s} KL[\mathcal{D}(\mathbf{p}_i|\tilde{\boldsymbol{\alpha}}_i)||\mathcal{D}(\mathbf{p}_i|\mathbf{1})], \quad (8)$$

where $\lambda_t = \min(1.0, t/10) \in [0, 1]$ is the annealing coefficient, t is the index of the current training epoch.

Without introducing additional model parameters, the uncertainty for prediction is directly calculated by:

$$u = \frac{K}{S_i} \quad (9)$$

according to the Subjective Logic framework, where $S_i = \sum_{k=1}^K \hat{\alpha}_{ik}$ is the total evidence of sample i .

D. Final Loss Function for UDA with Uncertainty

The final loss of the proposed method combines the original loss of the UDA task in Equation (1) and the evidential loss in Equation (8):

$$L = L_{uda} + \lambda_3 L_{evi} = \lambda_1 L_{cls} + \lambda_2 L_d + \lambda_3 L_{evi}, \quad (10)$$

where λ_1 , λ_2 and λ_3 balance the three loss components. In our experiments, λ_1 and λ_2 are directly set the same as the optimal ones given in [44] and optimal λ_3 is found empirically by the Target Risk (TGT) [44] by leaving out a subset of target domain samples and their labels as a validation set.

IV. EXPERIMENTS

A. Datasets and Evaluation Metrics

UCIHAR: The UCIHAR dataset [45] is collected using three types of sensors—an accelerometer, a gyroscope, and body sensors—attached to 30 subjects. Each subject performed six activities: walking, walking upstairs, walking downstairs, standing, sitting, and lying down. Due to the variability among

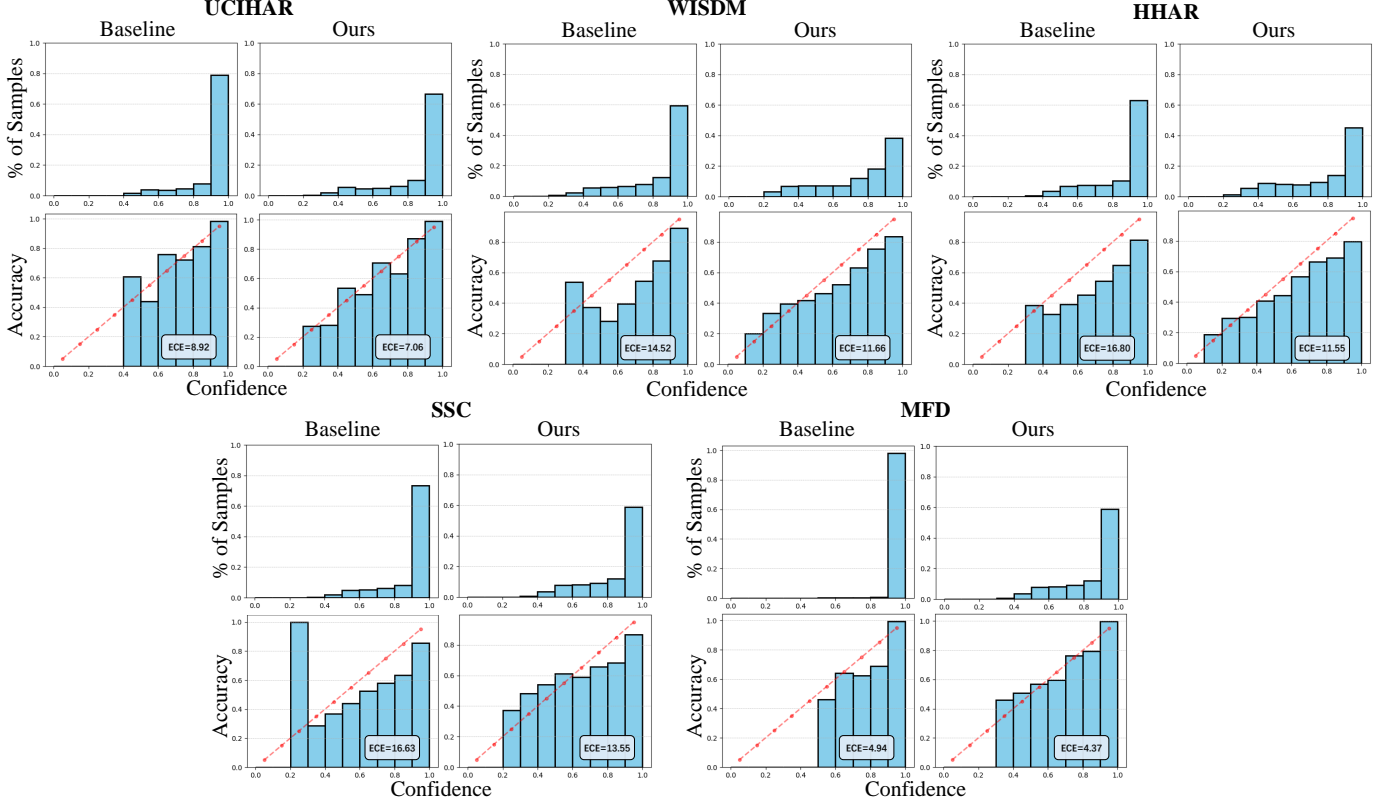


Fig. 7: The Expected Calibration Error (ECE) metric. The DDC method served as a baseline for experiments on five datasets. Each subplot's first row indicates the proportion of samples at different confidence levels predicted by the model relative to the total number of samples. The second row illustrates the discrepancy between the classification accuracy (blue bars) and the calibration probability (red dots) for samples at various confidence levels.

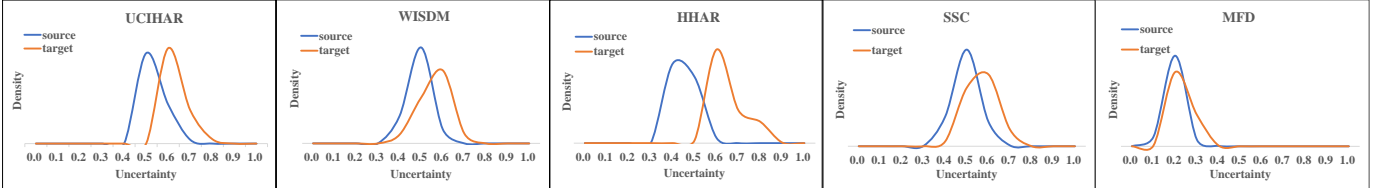


Fig. 8: Density of uncertainty. The baseline is the basic model without domain adaption, and add evidential to it to estimate uncertainty on both the source domain and target domain of UCIHAR, WISDM, HHAR, SSC and MFD datasets (data configuration is the same as AdaTime).

subjects, each is treated as a separate domain. Following the approach in AdaTime [19], we selected five scenarios for our study.

WISDM: Like UCIHAR, the WISDM dataset [46] employs accelerometer sensors but includes 36 subjects performing the same activities. It introduces challenges such as class imbalances, where data from certain subjects may lack some activity classes. Following AdaTime [19], we selected five cross-domain scenarios at random for analysis.

HHAR: The HHAR dataset [47], or Heterogeneity Human Activity Recognition, includes data from nine subjects using both smartphone and smartwatch sensors. We followed AdaTime [19] in utilizing five randomly selected cross-domain scenarios for our experiments.

SSC: The Sleep Stage Classification (SSC) involves categoriz-

ing EEG signals into five stages: Wake (W), three Non-Rapid Eye Movement (NREM) stages (N1, N2, N3), and Rapid Eye Movement (REM). We use the Sleep-EDF dataset [48], which contains EEG readings from 20 healthy subjects. We focused on a single EEG channel (Fpz-Cz) and included data from 10 subjects, setting up five cross-domain scenarios following prior research [19], [49] for controlled comparisons across EEG stages and subjects.

MFD: The Machine Fault Diagnosis (MFD) dataset from Paderborn University [50] is used for detecting faults via vibration signals under four distinct operating conditions, each treated as a separate domain. Our analysis involves five cross-condition scenarios to evaluate domain adaptation effectiveness, with each sample containing 5120 data points from a univariate channel, in line with previous methodologies [19].

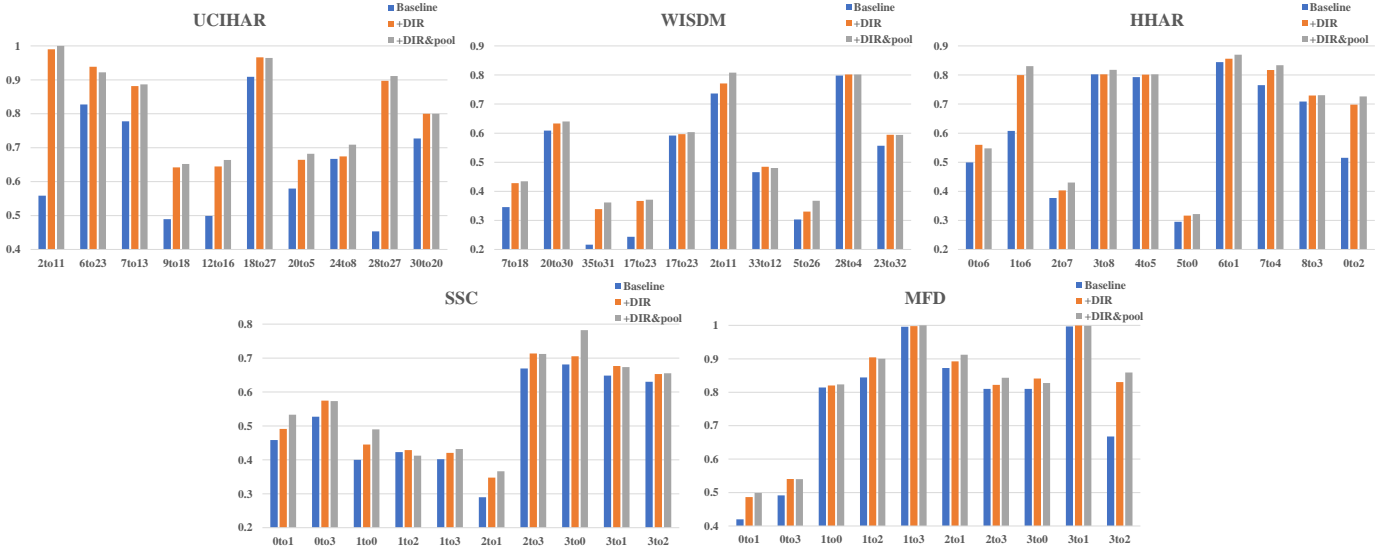


Fig. 9: Performance evaluation across different folds over 5 different datasets. The baseline is the basic model without domain adaption. Consistent performance improvements over different folds are found for all datasets.

Analysis of data distribution: Data distribution analyses are given in Figure 4 and Figure 5, where the label distributions and sample distributions after PCA for both source and target domains against different splits are visualized. It is clear that the UCIHAR and HHAR datasets have relatively uniform label distributions across various classes. In contrast, the other three datasets show more significant disparities among class label distributions. Additionally, the label distribution differences between the source and target domains for UCIHAR, HHAR, and MFD datasets are all less than 5%, indicating minimal overall variation. While the distribution differences of various categories between source and target domains in the WISDM and SSC datasets are significant, which partially explains why the F1 score for these datasets, shown later in Table II, are relatively low across different methods. The PCA visualization of sample distributions across different domain splits reveals substantial differences between source and target domains across multiple split configurations. This observation provides a strong motivation for domain adaptation strategies to align features across different domains, improving model robustness and generalization.

Evaluation Metric: Following previous methods [44], to verify the effectiveness of the proposed framework with uncertainty awareness, we use 12 baseline models, including the base model without domain alignment, DDC [11], Deep [51], HoMM [10], DANN [52], MMDA [53], DSAN [12], CDAN [14], DIRT [54], CoDATS [24], AdvSKM [55], SASA [56] and CLUDA [57]. The F1 score is reported as the evaluation metric to validate the performance.

B. The Impact of Uncertainty

1) *Impact on Prediction Accuracy:* The F1 scores of different baselines incorporated with uncertainty estimation are given in Table I, where uncertainty imposed by normal-inverse-gamma (NIG) prior [18] is used as a comparison. We

implemented all three different evidential losses aforementioned in Equation 4, Equation 5, and Equation 6, respectively. The Bayesian risk loss with cross-entropy shows the best F1 score on average. All baseline models when incorporated with uncertainty outperform their counterparts. Baseline models with Dirichlet prior (DIR) outperform those with NIG prior, possibly because DIR is better suited for classification tasks. A significant performance improvement is observed even when there is no domain alignment, which suggests that the awareness of uncertainty itself imposes the model ability of generalization and robustness for domain shift.

The detailed performance comparisons with the proposed method and the baseline model without domain adaptation are summarized in Figure 3 and Figure 9, where the averaged classification confusion matrix over all folds and the F1 score over different folds are given, respectively. Higher positive prediction rates are achieved while miss-classification rates are decreased as shown in Figure 3, especially for walk and upstairs labels in the UCIHAR dataset, downstairs and upstairs labels in the WISDM dataset, and bike and upstairs labels in the HHAR dataset. The corresponding uncertainty values of each label average over the samples and folds are shown in the third column, where a higher uncertainty value is observed for a prediction with a low F1 score. Figure 9 shows that our method consistently achieves higher F1 scores over all different folds.

2) *Impact on Feature Learning:* The distribution of learned features of baseline method DDC and our method are compared in Figure 10. In comparison to the baseline method, the inclusion of uncertainty awareness in our approach leads to a more concentrated aggregation of features belonging to the same category across different domains, which is particularly noticeable for categories 1 and 2. Additionally, it pushes apart the features from different categories, both within and between the source and target domains. This separation is especially evident for categories 3 and 4 in the target domain, and

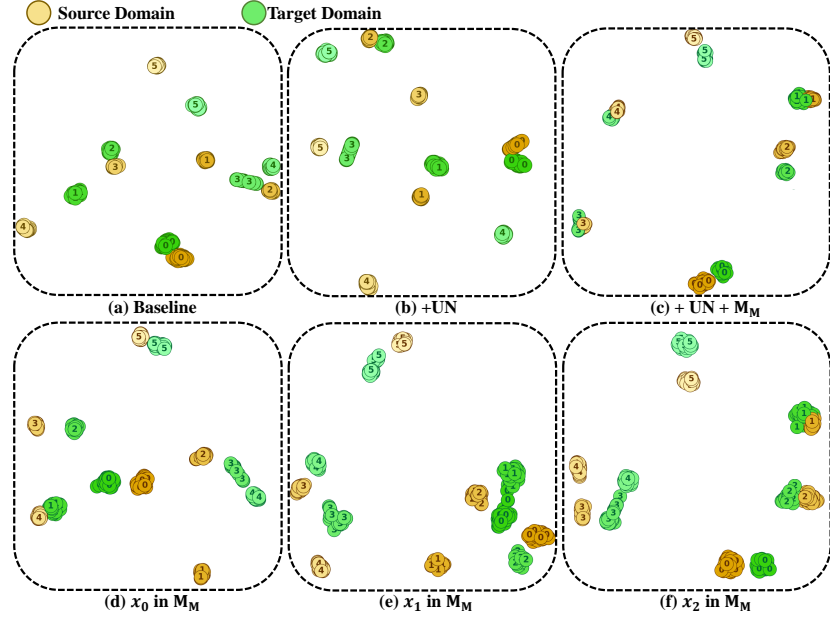


Fig. 10: The figure illustrates the t-SNE visualization results of features extracted by different methods and across various domains on the UCIHAR dataset's 2_to_11 fold. The numbers in the markers represent class indexes. Panels (a) to (f) display features extracted by different methods: (a) uses the DDC method as the baseline, (b) adds uncertainty estimation, (c) adds uncertainty estimation and a multi-scale mixing architecture with max-pooling. Panels (d) to (f) show different features in different scales from (c).

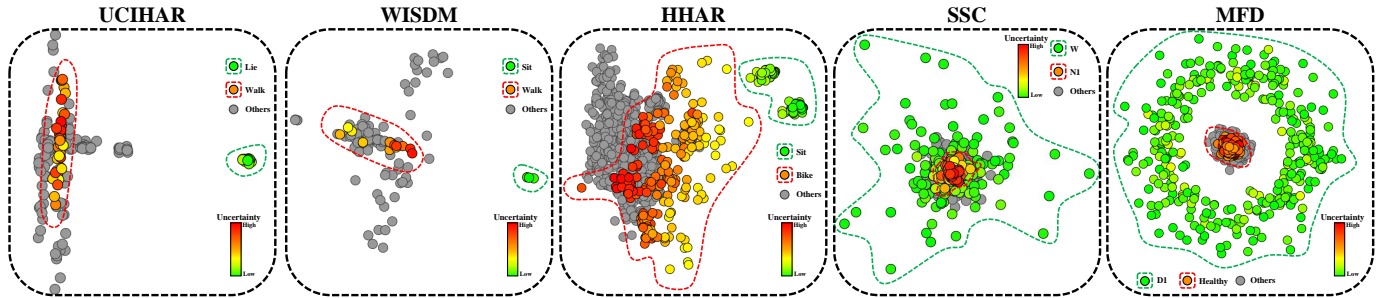


Fig. 11: The principal component analysis (PCA) visualization results of each sample and the uncertainty of some categories. The DDC [11] method was employed as a baseline for experiments on UCIHAR dataset's 6_to_23 fold, WISDM dataset's 33_to_12 fold, HHAR dataset's 4_to_6 fold, SSC dataset's 6_to_5 fold and MFD dataset's 0_to_3 fold.

categories 2 and 3 between the source and target domains.

C. The Impact of Multi-scale Mixing Architecture

Table II demonstrates that incorporating a multi-scale mixing architecture alongside uncertainty prediction significantly improves the average F1 scores of various baseline methods across different datasets. The results indicate that different down-sampling methods show varied performance across different datasets, the overall differences are minimal. Figure 10 (c) further shows that when the multi-scale mixing architecture is integrated, this aggregation of features from multiple domains is further improved. Moreover, within the multi-scale architecture, higher-level sequences demonstrate superior category aggregation, indicating the effectiveness of our approach in enhancing feature learning across scales as shown from Figure 10 (d) to (f).

To quantitatively illustrate the impact of multi-scale mixing on domain shift, we employ domain discrepancy metrics such as Maximum Mean Discrepancy (MMD) and Wasserstein Distance (WD) to measure the distance between the source and target domains when applying multi-scale mixing. The results, presented in the Tables III and IV, respectively, the tables demonstrate that multi-scale mixing effectively reduces domain discrepancy, as quantified by both WD and MMD. Specifically, multi-scale mixing with 1D CNNs shows notable success in minimizing MMD, whereas implementations using max or average pooling are particularly effective at reducing WD.

D. Model Performance Analysis

To demonstrate the calibration of our model compared to the baseline model, we examine two key perspectives across various datasets in the target domain. Firstly, we empirically

TABLE III: Effect of Multi-Scale Mixing Maximum Mean Discrepancy (MMD), the baseline method is DDC. While $+ M_L$ denotes the multi-scale mixing architecture with learnable parameter (1D CNN), $+ M_R$ denotes the multi-scale mixing architecture with random pooling, $+ M_M$ denotes the multi-scale mixing architecture with max pooling, $+ M_A$ denotes the multi-scale mixing architecture with averaging pooling

UCI HAR													
Split	2to11	6to23	7to13	9to18	12to16	18to27	20to5	24to8	28to27	30to20	Mean		
Baseline	0.236	0.259	0.252	0.219	0.302	0.234	0.226	0.288	0.244	0.262	0.252		
$+ M_L$	0.182	0.160	0.191	0.201	0.190	0.165	0.153	0.226	0.198	0.169	0.184		
$+ M_L + M_M$	0.162	0.161	0.231	0.276	0.203	0.211	0.180	0.209	0.221	0.170	0.202		
$+ M_R$	0.238	0.192	0.219	0.254	0.231	0.281	0.204	0.244	0.220	0.209	0.229		
$+ M_M$	0.215	0.217	0.199	0.248	0.255	0.254	0.194	0.239	0.243	0.203	0.227		
$+ M_A$	0.223	0.217	0.171	0.263	0.268	0.250	0.216	0.223	0.205	0.222	0.226		
WISDM													
Split	7to18	20to30	35to31	17to23	6to19	2to11	33to12	5to26	28to4	23to32	Mean		
Baseline	0.213	0.243	0.249	0.287	0.268	0.241	0.269	0.217	0.243	0.225	0.245		
$+ M_L$	0.144	0.182	0.194	0.180	0.241	0.141	0.243	0.195	0.141	0.199	0.186		
$+ M_L + M_M$	0.164	0.163	0.243	0.222	0.277	0.233	0.215	0.180	0.177	0.196	0.207		
$+ M_R$	0.205	0.226	0.213	0.263	0.233	0.237	0.330	0.214	0.200	0.275	0.240		
$+ M_M$	0.194	0.215	0.215	0.248	0.271	0.197	0.281	0.207	0.212	0.261	0.230		
$+ M_A$	0.221	0.223	0.184	0.241	0.266	0.214	0.281	0.180	0.179	0.261	0.225		
HHAR													
Split	0to6	1to6	2to7	3to8	4to5	5to0	6to1	7to4	8to3	9to2	Mean		
Baseline	0.185	0.183	0.174	0.194	0.214	0.206	0.172	0.230	0.204	0.191	0.195		
$+ M_L$	0.113	0.097	0.088	0.120	0.191	0.212	0.075	0.171	0.133	0.176	0.138		
$+ M_L + M_M$	0.202	0.120	0.157	0.131	0.213	0.136	0.157	0.189	0.187	0.146	0.164		
$+ M_R$	0.220	0.106	0.132	0.126	0.178	0.213	0.160	0.224	0.181	0.147	0.169		
$+ M_M$	0.188	0.143	0.133	0.161	0.184	0.185	0.153	0.204	0.149	0.185	0.168		
$+ M_A$	0.182	0.161	0.095	0.179	0.156	0.166	0.138	0.204	0.162	0.155	0.160		
SSC													
Split	0to11	7to18	9to14	12to5	16to1	3to19	18to12	13to17	5to15	6to2	Mean		
Baseline	0.185	0.109	0.093	0.114	0.116	0.107	0.118	0.162	0.144	0.112	0.126		
$+ M_L$	0.120	0.068	0.062	0.087	0.114	0.084	0.062	0.200	0.052	0.091	0.094		
$+ M_L + M_M$	0.200	0.109	0.061	0.082	0.107	0.055	0.057	0.203	0.118	0.126	0.112		
$+ M_R$	0.181	0.110	0.065	0.128	0.129	0.133	0.124	0.169	0.107	0.063	0.121		
$+ M_M$	0.186	0.083	0.075	0.084	0.093	0.112	0.118	0.187	0.095	0.103	0.114		
$+ M_A$	0.153	0.104	0.051	0.088	0.099	0.122	0.118	0.187	0.105	0.070	0.110		
MFD													
Split	0to1	0to3	1to0	1to2	1to3	2to1	2to3	3to0	3to1	3to2	Mean		
Baseline	0.221	0.223	0.247	0.257	0.124	0.196	0.183	0.224	0.140	0.254	0.207		
$+ M_L + M_M$	0.183	0.184	0.182	0.219	0.086	0.135	0.136	0.172	0.057	0.205	0.156		
$+ M_R$	0.204	0.208	0.198	0.150	0.071	0.168	0.173	0.215	0.064	0.160	0.161		
$+ M_M$	0.165	0.169	0.192	0.179	0.061	0.144	0.136	0.184	0.068	0.179	0.148		
$+ M_A$	0.173	0.193	0.198	0.190	0.079	0.128	0.139	0.206	0.060	0.208	0.157		

analyze the relationship between uncertainty estimates and prediction F1 scores. Secondly, we evaluate the Expected Calibration Error (ECE) metric.

1) *Uncertainty vs F1*: Our experiment results, as depicted in Figure 6, consistently demonstrate that uncertainty values exhibit a roughly linear inverse relationship with the F1 score across all five datasets. This suggests a broader phenomenon rather than being specific to particular data types. Lower uncertainty values correspond to higher confidence in model predictions. Conversely, when the model tends to make less accurate predictions, resulting in lower F1 scores, our model produces higher uncertainty values. This indicates that the uncertainty is well-calibrated.

2) *Expected Calibration Error*: The Expected Calibration Error (ECE) metric measures the discrepancy between the predicted probabilities and the true probabilities of the model. It provides a holistic assessment of the model’s calibration performance across different confidence levels. The ECE metrics for different datasets are given in Figure 7.

E. Uncertainty Density between Domains

The byproduct of our method is to quantify the uncertainty of the prediction. Illustrations of the uncertainty density of the prediction on the source and target domain of different

TABLE IV: Effect of Multi-Scale Mixing on Wasserstein Distance (WD), the baseline method is DDC. While $+ M_L$ denotes the multi-scale mixing architecture with learnable parameter (1D CNN), $+ M_R$ denotes the multi-scale mixing architecture with random pooling, $+ M_M$ denotes the multi-scale mixing architecture with max pooling, $+ M_A$ denotes the multi-scale mixing architecture with averaging pooling

UCI HAR													
Method	2to11	6to23	7to13	9to18	12to16	18to27	20to5	24to8	28to27	30to20	Mean		
Baseline	11.74	15.39	14.74	23.30	34.00	21.10	21.37	18.22	9.44	27.59	19.69		
$+ M_L$	7.48	20.36	14.61	21.56	31.59	13.35	17.36	21.02	18.19	21.98	18.75		
$+ M_L + M_M$	7.62	19.79	15.28	21.56	31.80	15.43	17.68	21.49	17.91	22.86	19.14		
$+ M_R$	8.23	19.67	14.99	21.47	31.33	14.56	18.20	20.47	16.81	22.50	18.82		
$+ M_M$	7.81	19.34	14.98	21.03	31.68	13.71	17.41	20.74	16.90	22.06	18.57		
$+ M_A$	7.84	20.01	15.31	20.71	32.06	13.67	17.31	20.98	16.29	22.48	18.66		
WISDM													
Method	7to18	20to30	35to31	17to23	6to19	2to11	33to12	5to26	28to4	23to32	Mean		
Baseline	30.45	34.58	30.27	41.04	35.13	27.95	38.71	21.61	29.35	49.59	33.87		
$+ M_L$	27.26	29.57	25.00	21.45	37.79	27.60	28.93	14.40	31.10	34.22	27.73		
$+ M_L + M_M$	27.49	29.46	25.57	28.30	37.78	28.83	30.09	15.45	33.61	34.13	28.62		
$+ M_R$	25.95	30.55	25.29	22.72	36.33	27.41	29.34	15.22	31.66	33.32	27.78		
$+ M_M$	25.93	29.97	25.75	22.15	36.45	27.79	28.95	14.93	31.97	33.14	27.70		
$+ M_A$	26.08	29.40	24.92	22.82	36.91	27.44	29.38	14.16	31.27	33.13	27.55		
HHAR													
Method	0to6	1to6	2to7	3to8	4to5	5to0	6to1	7to4	8to3	9to2	Mean		
Baseline	58.10	36.35	48.10	31.87	37.71	82.69	32.58	43.09	39.58	44.80	45.49		
$+ M_L$	29.77	27.19	29.41	18.11	21.59	42.32	22.44	25.96	24.98	28.23	27.01		
$+ M_L + M_M$	32.77	31.20	31.71	18.36	25.28	45.02	21.33	24.35	25.59	30.39	28.60		
$+ M_R$	28.68	29.48	28.51	17.08	19.42	40.77	23.51	23.12	24.47	29.33	26.44		
$+ M_M$	28.01	28.31	28.18	17.05	20.51	41.34	22.39	22.64	23.68	27.74	25.98		
$+ M_A$	27.66	27.53	27.88	16.48	20.24	41.19	22.96	22.16	24.26	28.22	25.86		
SSC													
Method	0to11	7to18	9to14	12to5	16to1	3to19	18to12	13to17	5to15	6to2	Mean		
Baseline	13.02	5.37	4.04	5.76	4.22	4.73	6.30	7.17	10.37	4.50	6.55		
$+ M_L$	9.38	5.13	3.02	4.04	4.22	7.07	8.47	7.45	8.15	5.40	6.23		
$+ M_L + M_M$	9.40	5.74	3.65	4.33	4.61	6.79	9.24	7.02	7.83	5.91	6.45		
$+ M_R$	9.41	5.24	2.71	3.71	4.46	7.34	8.90	7.21	8.36	5.37	6.27		
$+ M_M$	9.54	5.41	2.92	4.14	4.44	6.62	8.72	7.04	7.86	5.47	6.22		
$+ M_A$	9.84	5.88	2.30	3.65	4.01	7.01	8.78	6.89	7.65	5.34	6.14		
MFD													
Method	0to1	0to3	1to0	1to2	1to3	2to1	2to3	3to0	3to1	3to2	Mean		
Baseline	17.82	17.04	21.79	14.27	1.21	9.39	8.10	19.24	1.75	16.27	12.69		
$+ M_L$	8.35	7.88	11.44	8.53	4.55	4.95	2.02	10.69	2.12	5.76	6.63		
$+ M_L + M_M$	12.71	7.30	9.67	8.99	2.30	6.21	5.47	9.81	1.78	7.00	7.12		
$+ M_R$	8.97	4.06	9.07	5.88	0.98	3.87	2.57	8.34	1.				

categories with moderate to high uncertainty. This suggests that “Bike” samples are relatively more difficult to classify.

V. CONCLUSION

In this paper, we propose evidential learning in the framework of unsupervised domain adaptation for human activity recognition tasks. The uncertainty is incorporated using the network output via evidential loss without any additional network parameters to optimize the Bayesian risk under the Dirichlet prior to labels. The awareness of the uncertainty in the model prediction helps to learn features that are better aligned for source and target domains and thus show better generation ability in the target domain. Furthermore, we introduce a multi-scale mixing architecture to further enhance the model’s performance. Extensive experiments conducted on 5 datasets and 12 baseline methods demonstrate that our proposed method enhances the robustness of the model in domain shift scenarios. Extensive analysis was conducted on the impact of uncertainty on feature distribution, revealing insights into how uncertainty influences feature alignment across different domains and enhances model robustness to domain shifts. Additionally, our analysis of the relationship between sample uncertainty and PCA of sample distributions indicates a strong association between uncertainty and sample difficulty. The PCA results show that higher uncertainty often corresponds to more challenging samples, suggesting a meaningful link between uncertainty levels and sample complexity.

ACKNOWLEDGMENT

This work was supported by the Natural Science Foundation of Jiangxi Province (Grant No. 20223AEI91002). It was also partially supported by the National Natural Science Foundation of China (Grant No. 62461028) and the China Postdoctoral Science Foundation (Grant No. 2024T170364).

APPENDIX

A. Comparison of Monte Carlo Uncertainty

In addition to our evidential learning-based uncertainty, we also study uncertainty estimated using Monte Carlo (MC) dropout shown in Figure 12. The results demonstrate that our method provides more interpretable uncertainty, exhibiting a stronger correlation with the F1 score compared to the MC approach.

B. The Notational Summary Table

We have show the Notational Summary in Table V.

C. The Statistical Details of the Dataset

The statistical details of the dataset, such as the classes and domains are summarized in the following tables (VI, VII, VIII, IX, X) for ease of reference.

D. The Details of the down-sampling Methods

Parameters of the different down-sampling methods are summarized in Table XI.

TABLE V: Notational summary of the unsupervised domain adaptation framework

Symbol	Description
X_s	Source domain data
Y_s	Labels for source domain data
X_t	Target domain data (unlabeled)
\mathcal{L}_d	Domain loss
\mathcal{L}_{cls}	Classification loss on the source domain
\mathcal{L}_{levi}	Evidential loss for uncertainty estimation
$f(\theta)$	Feature extractor
$h(\theta)$	Classifier
α	Dirichlet distribution parameters
K	Total number of classes
N_s, N_t	Number of samples in source and target domains

E. Domain Adaptation Loss

A table summarizing the expressions of different L_d for various domain adaptation methods is provided in Table XII.

F. Limitations

While the proposed method demonstrates good performance and interpretability, several limitations remain. First, as shown in Table XIII, the computational cost of the model—particularly during training—may be significant due to the complexity of the architecture and the need for uncertainty estimation. This may limit its applicability in resource-constrained environments or real-time settings. Exploring more efficient approximations or lightweight model variants could help mitigate this overhead. Secondly, the methods can be further evaluated in more challenging real-world scenarios, such as variations across different scanners, institutions, and patient populations.

REFERENCES

- [1] H. Ismail Fawaz, G. Forestier, J. Weber, L. Idoumghar, and P.-A. Muller, “Deep learning for time series classification: a review,” *Data mining and knowledge discovery*, vol. 33, no. 4, pp. 917–963, 2019.
- [2] Y. Chang, A. Mathur, A. Isopoussu, J. Song, and F. Kawsar, “A systematic study of unsupervised domain adaptation for robust human-activity recognition,” *Proceedings of the ACM on Interactive, Mobile, Wearable and Ubiquitous Technologies*, vol. 4, no. 1, pp. 1–30, 2020.
- [3] D. Roggen, A. Calatroni, M. Rossi, T. Holleczek, K. Förster, G. Tröster, P. Lukowicz, D. Bannach, G. Pirk, A. Ferscha *et al.*, “Collecting complex activity datasets in highly rich networked sensor environments,” in *Seventh international conference on networked sensing systems (INSS)*. IEEE, 2010, pp. 233–240.
- [4] E. Eldele, M. Ragab, Z. Chen, M. Wu, C.-K. Kwoh, X. Li, and C. Guan, “Adast: Attentive cross-domain eeg-based sleep staging framework with iterative self-training,” *IEEE Transactions on Emerging Topics in Computational Intelligence*, vol. 7, no. 1, pp. 210–221, 2022.
- [5] A. L. Goldberger, L. A. N. Amaral, L. Glass, J. M. Hausdorff, P. C. Ivanov, R. G. Mark, J. E. Mietus, G. B. Moody, C.-K. Peng, and H. E. Stanley, “Physiobank, physiotoolkit, and physionet components of a new research resource for complex physiologic signals,” *Circulation*, vol. 101, no. 23, pp. 215–220, 2000.
- [6] S. Niu, Y. Liu, J. Wang, and H. Song, “A decade survey of transfer learning (2010–2020),” *IEEE Transactions on Artificial Intelligence*, vol. 1, no. 2, pp. 151–166, 2020.
- [7] C. Wang, C. Xu, and D. Tao, “Self-supervised pose adaptation for cross-domain image animation,” *IEEE Transactions on Artificial Intelligence*, vol. 1, no. 1, pp. 34–46, 2020.
- [8] H. Wu and M. K. Ng, “Multiple graphs and low-rank embedding for multi-source heterogeneous domain adaptation,” *ACM Transactions on Knowledge Discovery from Data (TKDD)*, vol. 16, no. 4, pp. 1–25, 2022.
- [9] B. Sun and K. Saenko, “Deep coral: Correlation alignment for deep domain adaptation,” in *ECCV*. Springer, 2016, pp. 443–450.

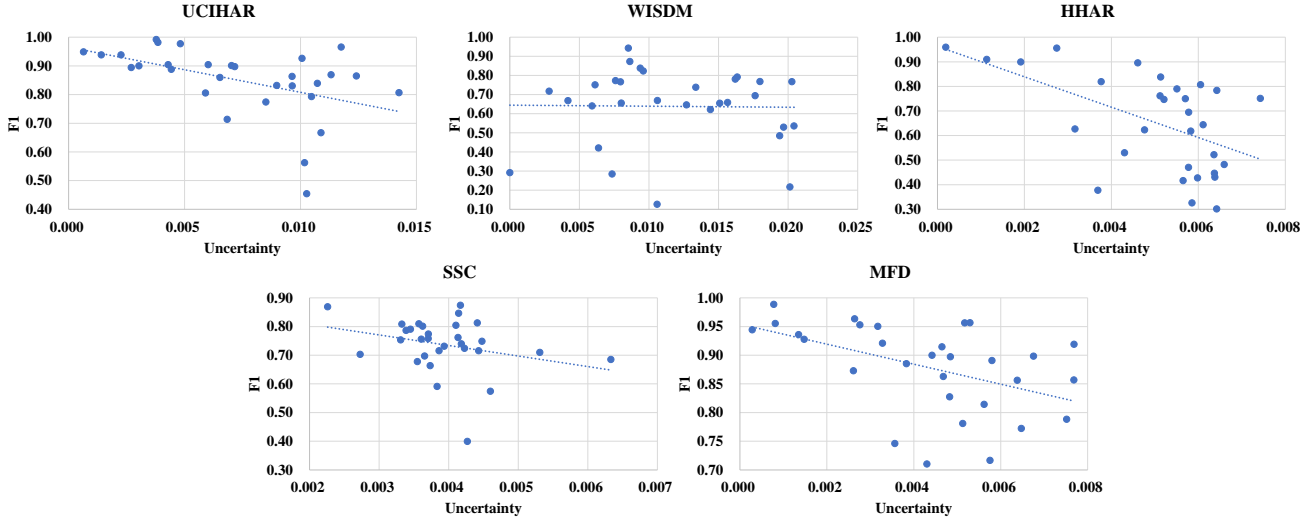


Fig. 12: The correlation between F1 score and Monte Carlo uncertainty. The baseline is the basic model without domain adaption, randomly select 30 folds on UCIHAR, WISDM, HHAR, SSC and MFD datasets for test, each fold test 100 times. The x axis is the uncertainty obtained by MC dropout, and the y axis is the mean of the F1 score.

- [10] C. Chen, Z. Fu, Z. Chen, S. Jin, Z. Cheng, X. Jin, and X.-S. Hua, “Homm: Higher-order moment matching for unsupervised domain adaption,” *AAAI*, 2020.
- [11] E. Tzeng, J. Hoffman, N. Zhang, K. Saenko, and T. Darrell, “Deep domain confusion: Maximizing for domain invariance,” *arXiv preprint arXiv:1412.3474*, 2014.
- [12] Y. Zhu, F. Zhuang, J. Wang, G. Ke, J. Chen, J. Bian, H. Xiong, and Q. He, “Deep subdomain adaptation network for image classification,” *IEEE Transactions on Neural Networks and Learning Systems*, vol. 32, no. 4, pp. 1713–1722, 2021.
- [13] Y. Ganin, E. Ustinova, H. Ajakan, P. Germain, H. Larochelle, F. Laviolette, M. March, and V. Lempitsky, “Domain-adversarial training of neural networks,” 2016.
- [14] M. Long, Z. Cao, J. Wang, and M. I. Jordan, “Conditional adversarial domain adaptation,” in *NeurIPS*, 2018.
- [15] M. Ragab, E. Eldele, Z. Chen, M. Wu, C.-K. Kwoh, and X. Li, “Self-supervised autoregressive domain adaptation for time series data,” *IEEE Transactions on Neural Networks and Learning Systems*, pp. 1–11, 2022.
- [16] Q. Liu and H. Xue, “Adversarial spectral kernel matching for unsupervised time series domain adaptation,” in *Proceedings of the Thirtieth International Joint Conference on Artificial Intelligence, IJCAI-21*, Z.-H. Zhou, Ed. International Joint Conferences on Artificial Intelligence Organization, 8 2021, pp. 2744–2750.
- [17] M. Sensoy, L. M. Kaplan, and M. Kandemir, “Evidential deep learning to quantify classification uncertainty,” in *NeurIPS*, 2018, pp. 3179–3189.
- [18] A. Amini, W. Schwarting, A. Soleimany, and D. Rus, “Deep evidential regression,” *NeurIPS*, vol. 33, pp. 14927–14937, 2020.
- [19] M. Ragab, E. Eldele, W. L. Tan, C.-S. Foo, Z. Chen, M. Wu, C. K. Kwoh, and X. Li, “Adatime: A benchmarking suite for domain adaptation on time series data,” *arXiv preprint arXiv:2203.08321*, 2022.
- [20] W. Liu, X. Zhong, L. Wang, J. Hou, Y. Luo, J. Yan, and Y. Fang, “Uncertainty awareness for unsupervised domain adaptation on human activity recognition,” in *International Joint Conference on Artificial Intelligence*. Springer, 2024, pp. 85–98.
- [21] C. Lessmeier, J. K. Kimotho, D. Zimmer, and W. Sextro, “Condition monitoring of bearing damage in electromechanical drive systems by using motor current signals of electric motors: A benchmark data set for data-driven classification,” in *PHM Society European Conference*, vol. 3, 2016, pp. 05–08.
- [22] B. Sun, J. Feng, and K. Saenko, “Return of frustratingly easy domain adaptation,” in *AAAI*, 2016.
- [23] S. J. Pan, I. W. Tsang, J. T. Kwok, and Q. Yang, “Domain adaptation via transfer component analysis,” *IEEE transactions on neural networks*, vol. 22, no. 2, pp. 199–210, 2010.
- [24] G. Wilson, J. R. Doppa, and D. J. Cook, “Multi-source deep domain adaptation with weak supervision for time-series sensor data,” in *SIGKDD*, 2020.
- [25] C. Cai, Y. Fang, W. Liu, R. Jin, J. Cheng, and Z. Chen, “Fedcov: Enhanced trustworthy federated learning for machine rul prediction with continuous-to-discrete conversion,” *IEEE Transactions on Industrial Informatics*, 2024.
- [26] C. Cai, W. Liu, X. Xia, Z. Chen, and Y. Fang, “Bayesian uncertainty calibration for federated time series analysis,” *IEEE Transactions on Multimedia*, 2024.
- [27] W. Liu, Z. Wu, Y. Zhao, Y. Fang, C.-S. Foo, J. Cheng, and G. Lin, “Harmonizing base and novel classes: A class-contrastive approach for generalized few-shot segmentation,” *International Journal of Computer Vision*, vol. 132, no. 4, pp. 1277–1291, 2024.
- [28] B. Qin, F. Meng, X. Fang, G. Dai, S. Yuan, and B. Mu, “Cau: A causality attention unit for spatial-temporal sequence forecast,” *IEEE Transactions on Multimedia*, 2023.
- [29] W. Liu, C. Zhang, G. Lin, and F. Liu, “Crnet: Cross-reference networks for few-shot segmentation,” in *CVPR*, 2020, pp. 4165–4173.
- [30] S. Purushotham, W. Carvalho, T. Nilanon, and Y. Liu, “Variational recurrent adversarial deep domain adaptation,” in *ICLR*, 2017.
- [31] G. Wilson, J. R. Doppa, and D. J. Cook, “Multi-source deep domain adaptation with weak supervision for time-series sensor data,” *Proceedings of the 26th ACM SIGKDD International Conference on Knowledge Discovery & Data Mining*, 2020.
- [32] R. Cai, J. Chen, Z. Li, W. Chen, K. Zhang, J. Ye, Z. Li, X. Yang, and Z. Zhang, “Time series domain adaptation via sparse associative structure alignment,” *ArXiv*, vol. abs/2205.03554, 2021.
- [33] F. Ott, D. Rügamer, L. Heublein, B. Bischl, and C. Mutschler, “Domain adaptation for time-series classification to mitigate covariate shift,” *Proceedings of the 30th ACM International Conference on Multimedia*, 2022.
- [34] X. Jin, Y. Park, D. Maddix, H. Wang, and Y. Wang, “Domain adaptation for time series forecasting via attention sharing,” in *Proceedings of the 39th International Conference on Machine Learning*, ser. Proceedings of Machine Learning Research, K. Chaudhuri, S. Jegelka, L. Song, C. Szepesvari, G. Niu, and S. Sabato, Eds., vol. 162. PMLR, 17–23 Jul 2022, pp. 10 280–10 297.
- [35] Y. Ozyurt, S. Feuerriegel, and C. Zhang, “Contrastive learning for unsupervised domain adaptation of time series,” *ArXiv*, vol. abs/2206.06243, 2022.
- [36] G. Wilson, J. R. Doppa, and D. J. Cook, “Calda: Improving multi-source time series domain adaptation with contrastive adversarial learning,” 2021.
- [37] T. Maekawa, D. Nakai, K. Ohara, and Y. Namioka, “Toward practical factory activity recognition: unsupervised understanding of repetitive assembly work in a factory,” in *Proceedings of the 2016 ACM International Joint Conference on Pervasive and Ubiquitous Computing*, 2016, pp. 1088–1099.
- [38] G. Yue, S. Zhang, T. Zhou, B. Jiang, W. Liu, and T. Wang, “Pyramid

TABLE VI: Class distribution of different training and test sets in the UCIHAR dataset. The correspondence between class indices and class names is as follows: 0-‘walk’, 1-‘upstairs’, 2-‘downstairs’, 3-‘sit’, 4-‘stand’, 5-‘lie’.

Train	Class Indices						Sum	Test	Class Indices						Sum
	0	1	2	3	4	5			0	1	2	3	4	5	
Split_1	66	37	34	33	37	35	242	Split_1	29	16	15	14	16	15	105
Split_2	41	34	33	32	38	33	211	Split_2	18	14	14	14	16	15	91
Split_3	41	41	34	36	43	43	238	Split_3	17	18	15	16	18	19	103
Split_4	42	36	31	35	39	38	221	Split_4	18	16	14	15	17	16	96
Split_5	39	33	33	31	39	36	211	Split_5	17	14	14	13	17	16	91
Split_6	40	36	33	38	40	40	227	Split_6	17	15	15	17	17	17	98
Split_7	40	36	33	33	37	36	215	Split_7	17	15	14	15	16	16	93
Split_8	33	29	26	32	38	38	196	Split_8	15	12	12	14	16	16	85
Split_9	36	34	29	35	32	35	201	Split_9	16	15	13	15	13	15	87
Split_10	37	33	26	38	31	40	205	Split_10	16	14	12	16	13	18	89
Split_11	41	38	32	37	33	40	221	Split_11	18	16	14	16	14	17	95
Split_12	35	36	32	36	43	42	224	Split_12	15	16	14	15	18	18	96
Split_13	40	38	33	34	40	43	228	Split_13	17	17	14	15	17	19	99
Split_14	41	38	31	38	42	36	226	Split_14	18	16	14	16	18	15	97
Split_15	38	34	29	41	37	50	229	Split_15	16	14	13	18	16	22	99
Split_16	36	36	33	48	54	49	256	Split_16	15	15	14	21	24	21	110
Split_17	43	33	32	45	54	50	257	Split_17	18	15	14	19	24	21	111
Split_18	39	41	38	40	51	45	254	Split_18	17	17	17	17	22	20	110
Split_19	37	28	27	51	51	58	252	Split_19	15	12	12	22	22	25	108
Split_20	36	36	31	46	51	47	247	Split_20	15	15	14	20	22	21	107
Split_21	36	33	32	59	62	63	285	Split_21	16	14	13	26	27	27	123
Split_22	32	30	25	43	44	50	224	Split_22	14	12	11	19	19	22	97
Split_23	41	36	38	48	47	50	260	Split_23	18	15	16	20	21	22	112
Split_24	41	41	38	48	48	50	266	Split_24	17	18	17	20	21	22	115
Split_25	52	45	41	45	52	51	286	Split_25	22	20	17	20	22	22	123
Split_26	41	38	35	55	52	53	274	Split_26	18	17	15	23	22	23	118
Split_27	40	35	31	49	56	52	263	Split_27	17	16	13	21	24	22	113
Split_28	38	36	32	50	55	56	267	Split_28	16	15	14	22	24	24	115
Split_29	37	34	34	42	45	48	240	Split_29	16	15	14	18	20	21	104
Split_30	46	46	43	43	41	49	268	Split_30	19	19	19	19	18	21	115

network with quality-aware contrastive loss for retinal image quality assessment,” *IEEE Transactions on Medical Imaging*, 2024.

[39] W. Liu, W. Zhou, J. Liu, P. Hu, J. Cheng, J. Han, and W. Lin, “Modality-aware feature matching: A comprehensive review of single-and cross-modality techniques,” *arXiv preprint arXiv:2507.22791*, 2025.

[40] B. Lakshminarayanan, A. Pritzel, and C. Blundell, “Simple and scalable predictive uncertainty estimation using deep ensembles,” in *NeurIPS*, 2017, pp. 6402–6413.

[41] J. Antorán, J. U. Allingham, and J. M. Hernández-Lobato, “Depth uncertainty in neural networks,” in *NeurIPS*, 2020, pp. 10 620–10 634.

[42] J. van Amersfoort, L. Smith, Y. W. Teh, and Y. Gal, “Uncertainty estimation using a single deep deterministic neural network,” in *ICML*, 2020, pp. 9690–9700.

[43] M. C. Mozer, “Induction of multiscale temporal structure,” *Advances in neural information processing systems*, vol. 4, 1991.

[44] M. Ragab, E. Eldele, W. L. Tan, C.-S. Foo, Z. Chen, M. Wu, C.-K. Kwoh, and X. Li, “Adatime: A benchmarking suite for domain adaptation on time series data,” *ACM Transactions on Knowledge Discovery from Data*, vol. 17, no. 8, pp. 1–18, 2023.

[45] D. Anguita, A. Ghio, L. Oneto, X. Parra, and J. L. Reyes-Ortiz, “A public domain dataset for human activity recognition using smartphones,” in *European Symposium on Artificial Neural Networks*, 2013, pp. 437–442.

[46] J. R. Kwapisz, G. M. Weiss, and S. A. Moore, “Activity recognition using cell phone accelerometers,” *Sigkdd Explorations*, vol. 12, no. 2, pp. 74–82, 2011.

[47] A. Stisen, H. Blunck, S. Bhattacharya, T. S. Prentow, M. B. Kjergaard, A. Dey, T. Sonne, and M. M. Jensen, “Smart devices are different: Assessing and mitigating mobile sensing heterogeneities for activity recognition,” in *Proceedings of the 13th ACM Conference on Embedded Networked Sensor Systems*, 2015, pp. 127–140.

[48] A. L. Goldberger, L. Amaral, L. Glass, J. M. Hausdorff, R. G. Ivanov, P. Mark, J. E. Mietus, G. B. Moody, C. Peng, and H. E. Stanley, “Physiobank, physiotoolkit, and physionet: components of a new research resource for complex physiologic signals,” *Circulation*, vol. 101, no. 23, pp. e215–e220, 2000.

[49] E. Eldele, Z. Chen, C. Liu, M. Wu, C.-K. Kwoh, X. Li, and C. Guan, “An attention-based deep learning approach for sleep stage classification with single-channel eeg,” *IEEE Transactions on Neural Systems and Rehabilitation Engineering*, vol. 29, pp. 809–818, 2021.

[50] C. Lessmeier, J. K. Kimotho, D. Zimmer, and W. Sextro, “Condition monitoring of bearing damage in electromechanical drive systems by using motor current signals of electric motors: A benchmark data set

for data-driven classification,” in *PHM Society European Conference*, vol. 3, no. 1, 2016.

[51] B. Sun, J. Feng, and K. Saenko, “Correlation alignment for unsupervised domain adaptation,” in *Domain Adaptation in Computer Vision Applications*. Springer, 2017, pp. 153–171.

[52] Y. Ganin, E. Ustinova, H. Ajakan, P. Germain, H. Larochelle, F. Laviolette, M. Marchand, and V. Lempitsky, “Domain-adversarial training of neural networks,” *JMLR*, vol. 17, no. 1, pp. 1–35, 2016.

[53] M. M. Rahman, C. Fookes, M. Baktashmotlagh, and S. Sridharan, *On Minimum Discrepancy Estimation for Deep Domain Adaptation*. Cham: Springer International Publishing, 2020, pp. 81–94.

[54] R. Shu, H. Bui, H. Narui, and S. Ermon, “A dirt-t approach to unsupervised domain adaptation,” in *International Conference on Learning Representations*, 2018.

[55] Q. Liu and H. Xue, “Adversarial spectral kernel matching for unsupervised time series domain adaptation,” in *Proceedings of the Thirtieth International Joint Conference on Artificial Intelligence, IJCAI-21*, 08 2021, pp. 2744–2750.

[56] R. Cai, J. Chen, Z. Li, W. Chen, K. Zhang, J. Ye, Z. Li, X. Yang, and Z. Zhang, “Time series domain adaptation via sparse associative structure alignment,” in *Proceedings of the AAAI Conference on Artificial Intelligence*, vol. 35, 2021, pp. 6859–6867.

[57] Y. Ozyurt, S. Feuerriegel, and C. Zhang, “Contrastive learning for unsupervised domain adaptation of time series,” *arXiv preprint arXiv:2206.06243*, 2022.

TABLE VII: Class distribution of different training and test sets in the WISDM dataset. The correspondence between class indices and class names is as follows: 0-‘walk’, 1-‘jog’, 2-‘sit’, 3-‘stand’, 4-‘upstairs’, 5-‘downstairs’.

Train	WISDM						Sum	Class Indices						Sum	
	Class Indices							0	1	2	3	4	5		
	0	1	2	3	4	5									
Split_0	12	48	0	0	13	56	129	Split_0	7	26	0	0	7	30	70
Split_1	0	51	0	0	0	51	102	Split_1	0	28	0	0	0	27	55
Split_2	15	48	6	12	14	57	152	Split_2	7	26	4	7	8	30	82
Split_3	7	3	5	0	6	26	47	Split_3	4	2	3	0	3	14	26
Split_4	14	28	7	7	14	53	123	Split_4	7	15	4	3	8	29	66
Split_5	7	51	7	3	7	53	128	Split_5	3	28	4	1	4	29	69
Split_6	10	40	10	10	15	48	133	Split_6	5	21	6	5	9	26	72
Split_7	14	45	12	14	19	74	178	Split_7	8	24	6	8	10	40	96
Split_8	0	0	0	0	0	56	56	Split_8	0	0	0	0	0	30	30
Split_9	16	53	0	6	18	57	150	Split_9	9	28	0	4	10	30	81
Split_10	11	54	0	0	19	52	136	Split_10	6	29	0	0	10	29	74
Split_11	12	53	10	7	11	47	140	Split_11	7	29	5	4	6	25	76
Split_12	18	54	5	6	20	57	160	Split_12	10	29	3	4	11	30	87
Split_13	12	57	0	0	35	61	165	Split_13	7	31	0	0	19	32	89
Split_14	7	56	0	0	9	50	122	Split_14	4	30	0	0	5	27	66
Split_15	7	0	13	8	6	54	88	Split_15	4	0	7	5	3	29	48
Split_16	16	12	0	0	25	42	95	Split_16	9	7	0	0	13	22	51
Split_17	10	52	7	8	10	54	141	Split_17	5	28	3	5	5	30	76
Split_18	11	71	10	9	18	77	196	Split_18	6	38	6	5	10	41	106
Split_19	20	57	68	23	21	57	246	Split_19	11	30	36	13	11	31	132
Split_20	18	41	6	12	21	54	152	Split_20	9	22	4	7	11	29	82
Split_21	16	27	0	0	23	30	96	Split_21	8	15	0	0	13	16	52
Split_22	8	53	0	0	21	29	111	Split_22	5	29	0	0	11	15	60
Split_23	12	53	3	2	13	26	109	Split_23	7	29	1	1	7	15	60
Split_24	0	28	0	0	0	29	57	Split_24	0	15	0	0	0	17	32
Split_25	16	52	0	0	16	57	141	Split_25	9	28	0	0	8	31	76
Split_26	15	53	9	6	14	54	151	Split_26	8	28	5	4	8	29	82
Split_27	13	0	0	5	12	62	92	Split_27	7	0	0	3	7	33	50
Split_28	18	55	10	7	21	54	165	Split_28	10	30	5	4	11	29	89
Split_29	17	0	6	14	18	54	109	Split_29	9	0	4	7	10	30	60
Split_30	17	61	9	11	20	73	191	Split_30	9	33	5	6	11	39	103
Split_31	10	53	13	7	16	53	152	Split_31	5	29	7	4	9	29	83
Split_32	19	13	14	6	10	65	127	Split_32	11	7	7	4	5	35	69
Split_33	12	56	6	6	17	58	155	Split_33	7	30	4	3	9	31	84
Split_34	0	55	6	5	0	30	96	Split_34	0	29	4	2	0	17	52
Split_35	18	53	10	9	23	27	140	Split_35	10	28	6	4	13	14	75

TABLE VIII: Class distribution of different training and test sets in the HHAR dataset. The correspondence between class indices and class names is as follows: 0-‘bike’, 1-‘sit’, 2-‘stand’, 3-‘walk’, 4-‘stairs up’, 5-‘stairs down’.

HHAR															
Train	Class Indices						Sum	Test	Class Indices						Sum
	0	1	2	3	4	5			0	1	2	3	4	5	
Split_0	209	166	185	158	156	192	1066	Split_0	89	71	79	68	67	83	457
Split_1	269	176	187	208	177	232	1249	Split_1	116	75	80	90	76	99	536
Split_2	192	160	185	185	174	210	1106	Split_2	83	69	79	80	74	90	475
Split_3	179	160	164	189	152	220	1064	Split_3	77	69	70	81	65	95	457
Split_4	239	159	187	189	168	227	1169	Split_4	102	68	81	81	72	97	501
Split_5	257	164	193	206	168	216	1204	Split_5	110	71	83	88	72	93	517
Split_6	214	167	191	173	183	239	1167	Split_6	91	72	82	74	79	103	501
Split_7	192	165	209	190	172	188	1116	Split_7	83	70	90	82	73	81	479
Split_8	239	151	208	216	162	219	1195	Split_8	103	65	89	92	70	94	513

TABLE IX: Class distribution of different training and test sets in the SSC dataset. The correspondence between class indices and class names is as follows: 0-‘W’, 1-‘N1’, 2-‘N2’, 3-‘N3’, 4-‘REM’.

SSC													
Train	Class Indices					Sum	Test	Class Indices					Sum
	0	1	2	3	4			0	1	2	3	4	
Split_0	259	82	436	362	238	1377	Split_0	112	35	187	155	102	591
Split_1	223	141	855	141	242	1602	Split_1	96	60	367	60	104	687
Split_2	177	194	663	150	239	1423	Split_2	76	84	284	64	103	611
Split_3	193	74	619	132	286	1304	Split_3	83	32	266	56	122	559
Split_4	269	212	794	103	326	1704	Split_4	116	91	340	44	140	731
Split_5	301	111	583	174	173	1342	Split_5	129	47	250	75	75	576
Split_6	234	102	577	186	202	1301	Split_6	101	44	247	79	87	558
Split_7	372	121	556	269	256	1574	Split_7	159	52	239	115	110	675
Split_8	327	75	413	442	274	1531	Split_8	140	32	178	190	117	657
Split_9	203	70	750	194	348	1565	Split_9	87	30	323	83	149	672
Split_10	209	127	895	22	284	1537	Split_10	90	55	383	9	122	659
Split_11	176	22	629	168	216	1211	Split_11	76	9	269	72	93	519
Split_12	326	118	525	131	320	1420	Split_12	140	51	225	56	137	609
Split_13	108	40	348	103	120	719	Split_13	47	17	149	44	52	309
Split_14	258	39	553	207	312	1369	Split_14	110	17	237	89	134	587
Split_15	685	62	554	248	350	1899	Split_15	294	26	238	107	150	815
Split_16	276	68	635	205	318	1502	Split_16	119	29	272	88	137	645
Split_17	605	46	710	282	299	1942	Split_17	260	19	305	121	128	833
Split_18	199	126	474	355	164	1318	Split_18	86	54	204	152	70	566
Split_19	395	133	887	119	432	1966	Split_19	169	57	380	51	186	843

TABLE X: Class distribution of different training and test sets in the MFD dataset. The correspondence between class indices and class names is as follows: 0-‘Healthy’, 1-‘D1’, 2-‘D2’.

MFD												
Train	Class Indices			Sum	Test	Class Indices			Sum			
	0	1	2			0	1	2				
Split_0	209	166	185	560	Split_0	89	71	79	239			
Split_1	269	176	187	632	Split_1	116	75	80	271			
Split_2	192	160	185	537	Split_2	83	69	79	231			
Split_3	179	160	164	503	Split_3	77	69	70	216			

TABLE XI: Down-Sampling Methods and Operations.

Method	Description	Operations
$+M_L$	Dual convolutional down-sampling.	‘Conv1d(C, 3, 2, 1, False)’
$+M_L + M_M$	Max pooling followed by convolutional down-sampling.	‘MaxPool1d(2)’, ‘Conv1d(C, 3, 2, 1, False)’
$+M_M$	Dual max pooling down-sampling.	‘MaxPool1d(2)’ twice
$+M_A$	Dual average pooling down-sampling.	‘AvgPool1d(2)’ twice
$+M_R$	Dual random-value down-sampling.	Random select, ‘MaxPool1d(2)’ twice

TABLE XII: For Deep CORAL, $\|\cdot\|_F^2$ denotes the squared Frobenius norm, C_S and C_T are covariance matrices of the source and target data. For HoMM, $n_s = n_t$ = batch size, $\phi_\theta(\cdot)$ denotes the activation function, \otimes denotes the outer product, and p denotes the p -level tensor. For DSAN, \mathcal{H} is the Reproducing Kernel Hilbert Space (RKHS) endowed with a characteristic kernel k . For DANN, $CE(\cdot)$ is the cross-entropy loss. For CDAN, \tilde{Y}_{ST} is the output predicted with the fusion of X_S and X_T , and Y_{ST} is the concatenated label. For DIRT, $f_\theta(\cdot)$ is the embedding function. For CoDATS, \mathcal{D}_{KL} is the Kullback-Leibler divergence. For AdvSKM and SASA, β is the associative strength distribution.

Method	Loss Name	Domain Adaptation Loss
DDC	MMD loss	$\left\ \frac{1}{n_S} \sum_{x_s \in X_S} \phi(x_s) - \frac{1}{n_T} \sum_{x_t \in X_T} \phi(x_t) \right\ $
Deep CORAL	Coral loss	$\frac{1}{4d^2} \ C_S - C_T\ _F^2$
HoMM	High-order MMD loss	$\frac{1}{L^p} \left\ \frac{1}{n_s} \sum_{i=1}^{n_s} \phi_\theta(x_s^i)^{\otimes p} - \frac{1}{n_t} \sum_{i=1}^{n_t} \phi_\theta(x_t^i)^{\otimes p} \right\ _F^2$
MMDA	MMD loss	$\left\ \frac{1}{n_S} \sum_{x_s \in X_S} \phi(x_s) - \frac{1}{n_T} \sum_{x_t \in X_T} \phi(x_t) \right\ $
	Coral loss	$\frac{1}{4d^2} \ C_S - C_T\ _F^2$
DSAN	Local MMD loss	$\mathbb{E}_c \left\ \mathbb{E}_{p(c)}[\phi(X_S)] - \mathbb{E}_{q(c)}[\phi(X_T)] \right\ _{\mathcal{H}}^2$
DANN	Domain loss	$CE(\hat{Y}_S, Y_S) + CE(\hat{Y}_T, Y_T)$
CDAN	Domain loss	$CE(\hat{Y}_{ST}, Y_{ST})$
DIRT	Domain loss	$\sup_D \left[\mathbb{E}_{x \sim D_S} \ln D(f_\theta(x)) + \mathbb{E}_{x \sim D_T} \ln(1 - D(f_\theta(x))) \right]$
CoDATS	Adversarial loss	$CE(F(X_S), Y_S) + \mathbb{E}_{X \sim D_T^X} \left[CE(F(X_T), Y_T) + \mathcal{D}_{KL}(Y_{\text{true}} \ \mathbb{E}_{X \sim D_T^X}[C(F(X))]) \right]$
AdvSKM	Adversarial MMD loss	$\sum_{i,j=1}^{N_S} \frac{K(\phi(x_i^s), \phi(x_j^s))}{N_S^2} + \sum_{i,j=1}^{N_T} \frac{K(\phi(x_i^t), \phi(x_j^t))}{N_T^2} - 2 \sum_{i=1}^{N_S} \sum_{j=1}^{N_T} \frac{K(\phi(x_i^s), \phi(x_j^t))}{N_S N_T}$
SASA	Domain loss	$\sum_{m=1}^M \left\ \frac{1}{n_S} \sum_{x_S \in X_S} \beta_T^m - \frac{1}{n_T} \sum_{x_T \in X_T} \beta_T^m \right\ $

TABLE XIII: The Floating Point Operations (FLOPs) of different methods measured at a batch size of 32.

	FLOPs (M)											
	noAdapt	DDC	Deep	HoMM	DANN	MMDA	DSAN	CDAN	DIRT	CoDATS	AdvSKM	SASA
baseline	29.20	58.39	58.39	58.39	58.47	58.39	58.39	59.07	58.55	59.48	59.18	58.70
$+UN$	29.20	58.39	58.39	58.39	58.47	58.39	58.39	59.07	58.55	59.48	59.18	58.70
$+UN + M_L$	53.39	106.78	106.78	106.79	107.09	106.78	106.79	108.49	107.42	115.20	108.35	108.04
$+UN + M_L + M_M$	53.37	106.74	106.74	106.75	107.06	106.74	106.75	108.46	107.38	115.16	108.32	108.00
$+UN + M_R$	53.36	106.71	106.71	106.72	107.03	106.71	106.72	108.43	107.35	115.13	108.29	107.97
$+UN + M_M$	53.36	106.71	106.71	106.72	107.03	106.71	106.72	108.43	107.35	115.13	108.29	107.97
$+UN + M_A$	53.36	106.71	106.71	106.72	107.03	106.71	106.72	108.43	107.35	115.13	108.29	107.97